

Physics-inspired pseudo-transient method and its application in modelling focused fluid flow with geological complexity

Lawrence Hongliang Wang,¹ Viktoriya M. Yarushina,¹ Yury Alkhimenkov^{2,3} and Yury Podladchikov^{2,3}

¹*Department of Reservoir Technology, Institute for Energy Technology, 2007 Kjeller, Norway. E-mail: hongliangw@ife.no*

²*Swiss Geocomputing Center, University of Lausanne, CH-1015 Lausanne, Switzerland*

³*Faculty of Mechanics and Mathematics, Lomonosov Moscow State University, Moscow 119991, Russia*

Accepted 2021 0. Received 2021 October 18; in original form 2021 May 27

SUMMARY

Two-phase flow equations that couple solid deformation and fluid migration have opened new research trends in geodynamic simulations and modelling of subsurface engineering. Physical non-linearity of fluid-rock systems and strong coupling between flow and deformation in such equations lead to interesting predictions such as spontaneous formation of focused fluid flow in ductile/plastic rocks. However, numerical implementation of two-phase flow equations and their application to realistic geological environments with complex geometries and multiple stratigraphic layers is challenging. This study documents an efficient pseudo-transient solver for two-phase flow equations and describes the numerical theory and physical rationale. We provide a simple explanation for all steps involved in the development of a pseudo-transient numerical scheme for various types of equations. Two different constitutive models are used in our formulations: a bilinear viscous model with decompaction weakening and a viscoplastic model that allows decompaction weakening at positive effective pressures. The resulting numerical models are used to study fluid leakage from high porosity reservoirs into less porous overlying rocks. The interplay between time-dependent rock deformation and the buoyancy of ascending fluids leads to the formation of localized channels. The role of material parameters, reservoir topology, geological heterogeneity and porosity is investigated. Our results show that material parameters control the propagation speed of channels while the geometry of the reservoir controls their locations. Geological layers present in the overburden do not stop the propagation of the localized channels but rather modify their width, permeability, and growth speed.

Key words: Permeability and porosity; geomechanics; numerical modelling; Pseudo-transient; viscoplastic rheology; creep and deformation.

1 INTRODUCTION

1.1 Fluid flow in solid earth

Many geological processes involve fluid flow coupled with solid rock deformation. Mantle convection models that consider only solid deformation have achieved great success in approaching geodynamic problems. However, demand has increased for resolving fluid flow and solid–fluid interaction in the last decade, as processes such as melt segregation, magma transport and/or fluid migration in subduction zones have come into attention (Mckenzie 1984; Cai & Bercovici 2013; Jordan *et al.* 2018; Petrini *et al.* 2020). Similarly, crustal processes, such as episodic tremor and slow slip on the faults, formation of focused fluid flow systems and pore fluid migration in sedimentary basins, also present an explicit

requirement for solving coupled deformation of solids and fluids (Audet & Fowler 1992; Rice 1992; Räss *et al.* 2018). Even engineering processes such as hydraulic fracturing, CO₂ storage in geological formations and geothermal energy extraction require consideration of porous flow in deforming rocks (Ji *et al.* 2009; Wangen 2011; Yarushina *et al.* 2013; Elenius *et al.* 2018; Tarokh *et al.* 2020).

The same physical process has been described to using several different terminologies in various fields, including two-phase flow (Bercovici *et al.* 2001; Katz *et al.* 2006; Schmeling & Wallner 2012; Keller *et al.* 2013; Zheng *et al.* 2016; Wang *et al.* 2019) or compaction-driven fluid flow (Connolly & Podladchikov 1998; Vasilyev *et al.* 1998; Yarushina & Podladchikov 2015; Omlin *et al.* 2018) in geodynamics; and coupled fluid flow or geomechanics in petroleum engineering (Morency *et al.* 2007; Ji *et al.* 2009).

The mathematical formulations of these approaches, though written differently, are based on the same physics and differ mostly in assumed rheological laws.

The formation of channel-like focused fluid flow is one of the most interesting findings of two-phase flow models. It has been discussed in the context of melt segregation in the asthenosphere (Connolly & Podladchikov 2007), petroleum migration (Appold & Nunn 2002), the genesis of mud volcanoes (Revil 2002), and formation of seismic chimneys (Räss *et al.* 2014). One important conclusion of these studies is that the asymmetry of the bulk viscosity for compaction and decompaction drives the formation of elongated fluid channels. The channel size and evolution depend on material parameters such as permeability, bulk, and shear viscosities. However, existing models consider simplified setups that are far from real-world applications. The effects of geological heterogeneity or geometry have not yet been studied. However, these factors have a profound influence on the formation of fluid channels. Here, we address these questions and show how other factors such as the host rock's porosity, rock properties, various geological layers and their geometries affect the formation and propagation of channels.

1.2 Numerical methods in geosciences

Conventional numerical methods, such as matrix-based finite element (FE), finite volume (FV) and finite difference (FD), face several challenges in solving multiphysics non-linear problems in geosciences. First, high-resolution 3-D modelling requires assembling large matrices that are challenging to solve even with the sparse matrix format (Burov *et al.* 2014; May *et al.* 2014; Morra 2020). As a result, the maximum degree of freedom is usually limited to $<10^9$ in published 3-D models (Zhong *et al.* 2000; Settari & Walters 2001; Tackley 2008; May *et al.* 2014; Moresi *et al.* 2014; Dannberg & Heister 2016; Spitz *et al.* 2020; Rinaldi *et al.* 2021). Secondly, existing porous flow models in deformable rocks commonly use simplified equations that might give inaccurate results (Settari & Walters 2001; Prevost 2014). Thirdly, non-linear physics, such as plastic deformation of the rock or stress-dependent permeability for the fluid flow, may lead to convergence problems (Yarushina *et al.* 2010; Duretz *et al.* 2018).

Matrix-free numerical methods that solve systems of partial differential equations (PDE) without assembling and storing the coefficient matrix have been used to model rock deformation since the pioneering works of Cundall (1989); Poliakov *et al.* (1993) and Burov *et al.* (2001). With the development of High-performance computing, matrix-free methods have shown a significant advantage over matrix-based methods in terms of both memory use and parallel efficiency (May *et al.* 2015; Bauer *et al.* 2019; Clevenger & Heister 2019; Duretz *et al.* 2019; Räss *et al.* 2019). Recent studies with matrix-free methods have demonstrated the ability to solve up to 10^{12} degrees of freedom with a parallel efficiency of >90 per cent (Bauer *et al.* 2019), which is far beyond what matrix-based methods can reach. At the same time, the iterative procedure of Pseudo-transient continuation, inspired by physical processes, has been proven to solve multiphysics problems efficiently (Frankel 1950; Calder & Yezzi 2019; Räss *et al.* 2019; Benyamin *et al.* 2020). With matrix-free implementation, Rass *et al.* 2019 applied a pseudo-transient solver to simulate the long-term evolution of large-scale 3-D problems (1000^3) and showed its ability to handle the non-linearity of Kozeny-Carman permeability and decompaction weakening. These studies confirmed that the matrix-free

pseudo-transient method can solve large-scale problems and handle the significant non-linearity of physical problems. Given the potential of this state-of-the-art approach, more studies are needed to explain the mathematical and physical foundation and demonstrate its flexibility and robustness with different physics and model setups.

Here, we report a matrix-free pseudo transient method to solve the non-linear physics of two-phase flow systems and explain it such that geoscience modellers could easily understand and use. Using Fourier analysis theory, we analyse the time evolution of general damped waves with different parameters and derive the fastest damping parameters leading to the steady-state solution. We then transform the two-phase flow equations into damped waves equations by adding pseudo-transient time derivatives and derive the best damping parameters. The robustness and flexibility of the resulting numerical schemes are tested on 1-D and 2-D numerical examples. This scheme is used to simulate the development of focused fluid flow in various setups with geological complexity.

2 MODEL FORMULATION

We use a set of two-phase flow equations that describe fluid migration through the compaction and decompaction of the solid matrix with viscous rheology. Each phase (solid + fluid) is assumed to be incompressible. Thus, the momentum balance equations for the composite material and pore-fluid are given below (Yarushina & Podladchikov 2015) :

$$\nabla_j (\bar{\tau}_{ij} - \bar{P}\delta_{ij}) - g_i \bar{\rho} = 0 \quad (1)$$

$$\nabla_i q_i^D = \nabla_i \left(\frac{k}{\eta_f} (\nabla_i P_e - \nabla_i \bar{P} - g_i \rho_f) \right). \quad (2)$$

Here \bar{P} and $\bar{\rho}$ are the total pressure and density ($\bar{X} = (1 - \phi)X_s + \phi X_f$), δ_{ij} is the Kronecker delta ($\delta_{ij} = [i = j]$), g_i is component of gravity acceleration vector, η_f is the fluid viscosity and P_e is the effective pressure ($P_e = \bar{P} - P_f$). Porosity-dependent permeability, $k = k_0 \left(\frac{\phi}{\phi_0}\right)^n$, accounts for non-linear coupling of flow and rock deformation (Costa 2006). Here, k_0 is the reference permeability at reference porosity ϕ_0 . All symbols and their descriptions are listed in Table 1.

This study considers two different types of rock rheology: viscous bi-linear and viscoplastic. The influence of elastic strains is ignored. In both viscous and viscoplastic rocks, the deviatoric total stress tensor $\bar{\tau}_{ij}$ is related to the strain rate tensor:

$$\bar{\tau}_{ij} = 2\mu_s \left(\frac{1}{2}(\nabla_i V_j + \nabla_j V_i) - \frac{1}{3}\delta_{ij}\nabla_i V_i \right), \quad (3)$$

where μ_s is the solid shear viscosity, which is much larger than fluid shear viscosity η_f . The (de)compaction of the solid depends on the pressure field and bulk viscosity, which can be written: (Yarushina *et al.* 2020):

$$\nabla_i V_i = - \frac{P_e - P_d}{(1 - \phi)\eta_\phi}, \quad (4)$$

where η_ϕ is the bulk viscosity and P_d is the dilation pressure. For pure viscous deformation, dilation pressure in eq. (4) equals 0 ($P_d = 0$) (Yarushina & Podladchikov 2015; Räss *et al.* 2019). For viscoplastic deformation, dilation pressure is closely related to the plastic failure in rocks and corresponds to the peak on the failure envelope separating compaction cap surface from shear failure line (Yarushina *et al.* 2020). The formulations of P_d and η_ϕ are given in Appendix A, which depend on porosity, effective pressure and shear

Table 1. Symbols and parameter values.

Variable name	Symbol	Value
Porosity	ϕ	
Background porosity ^a	ϕ_0	0.001,0.01,0.1
Solid density	ρ_s	2
Fluid density	ρ_f	1
Average density	$\bar{\rho}$	
Gravitational acceleration	g	0,1
Solid velocity	V_i	
Darcy velocity	q_i^D	
Fluid shear viscosity	η_f	1
Reference permeability	k_0	1
Reference bulk viscosity	$\eta_{\phi_0 \text{ or } \eta_c}$	1
Bulk viscosity	η_ϕ	
Solid shear viscosity	μ_s	
Deviatoric stress tensor	τ_{ij}	
Total pressure	\bar{P}	
Fluid pressure	P_f	
Dilation pressure	P_d	
Effective pressure transition zone ^a	λ_P	
Decompaction weakening factor ^a	R	100 (1–1000)
Viscosity ratio factor ^a	$C = \eta_c \frac{\phi_0}{\mu_s}$	
Permeability exponent	n_p	2–20
Porosity contrast	ϕ_A	0.5–9
Compaction length	δ_c	1
Characteristic time	δ_t	
Characteristic pressure	p_c	
Effective pressure	$P_e = \bar{P} - P_f$	
Rheological parameter ^b	Y	2, 1, 0.6
Rheological parameter ^b	p_0	2.7, 1.35, 0.81

^aThese default values are used if not otherwise stated: $\phi_0 = 0.01$, $R = 100$, $n_p = 3$, $C = 1$, $\lambda_P = 0.2\rho_s g \Delta z$.

^bThese rheological parameters for viscoplastic rheology are described in Appendix A and used in models for Fig. 9.

stress. With the item P_d in eq. (4), decompaction can occur at positive effective pressures ($P_e > 0$) for viscoplastic rocks. Hereafter we call it ‘viscoplastic rheology’.

For the simple asymmetric rheology that ignores the effects of shear stresses on the bulk viscosity, we adopt a hyperbolic tangent formulation of bulk viscosity (Connolly & Podladchikov 1998):

$$\eta_\phi = \eta_c \frac{\phi_0}{\phi} \left[1 + \frac{1}{2} \left(\frac{1}{R} - 1 \right) \left(1 + \tan h \left(-\frac{P_e}{\lambda_P} \right) \right) \right], \quad (5)$$

where η_c (or η_{ϕ_0}) represents the background/reference bulk viscosity (at $\phi = \phi_0$) at compaction regime, λ_P defines the transition zone between the compaction and decompaction and R represents the factor of bulk viscosity weakening from compaction to decompaction. Eq. (5) describes the so-called ‘viscous bilinear rheology.’

To study the effect of different ratios between bulk and shear viscosities, we introduce parameter C ($C = \eta_c \frac{\phi_0}{\mu_s}$), which is a property of the rock that depends on the geometry of the pore network, mineralogical composition and grain size (Takei & Katz 2013, Yarushina *et al.* 2020). Recent experiments by Sabitova *et al.* (2021) show that this parameter lies between 1 and 10 for sedimentary rocks such as sandstone and limestone. In our models, we assume $C = 1$ if not stated otherwise. We can vary C to obtain suitable viscosity ratios in our models.

For the time evolution of porosity field, we use the mass conservation equation of the form:

$$\frac{\partial \phi}{\partial t} = (1 - \phi) \nabla_i V_i \quad (6)$$

Eqs (1), (3) and (4) represent the Stokes equations for a viscous fluid. In two-phase models, they are coupled with Darcy law (2) for porous fluid flow and the mass conservation eq. (6).

Dimension analysis of the equations show that there are three independent scales:

$$\begin{aligned} \delta_c &= \sqrt{\frac{k_0 \eta_c}{\eta_f}} \\ \delta_t &= \frac{\delta_c \eta_f}{k_0 \Delta \rho g} \phi_0 \\ p_c &= \Delta \rho g \delta_c \end{aligned} \quad (7)$$

These are known as the compaction length (δ_c), the compaction time (δ_t) and characteristic compaction pressure (p_c). Note that we include the background porosity ϕ_0 in the timescale, allowing us to compare the non-dimensional time of wave propagation for models with different background porosities. The characteristic velocity scale can be calculated as $v_c = \frac{\delta_c}{\delta_t} = \frac{k_0 \Delta \rho g}{\mu_f \phi_0}$. These scales help us to understand the two-phase system and its applications.

3 PSEUDO-TRANSIENT CONTINUATION METHOD

Pseudo-transient (PT) continuation is a physics-inspired iterative method that solves the steady-state problem by adding pseudo-time derivative, through which the steady-state solution is progressively achieved via a pseudo-time stepping. This method is also widely known as the 2nd Richardson or relaxation method (Frankel

1950), dynamic relaxation method (Otter *et al.* 1966; Zhang & Yu 1989) and inertial method (Poliakov *et al.* 1993). Recently, a general framework for this type of numerical methods has been developed, known as ‘PDE acceleration’, which shows great potentials both for the forward and inverse modeling problems (Calder & Yezzi 2018; Benyamin *et al.* 2020). As demonstrated by previous studies, fast PT solvers usually involve 2nd time-derivatives or ‘damping factors’ (Frankel 1950; Zhang & Yu 1989; Chen 2009; Benyamin *et al.* 2020) that enable the iteration number to be linearly scaled with grid number in one direction. The iteration process mimics the damping process of the wave equations ($dt \sim dx$) instead of the diffusion process ($dt \sim dx^2$). With numerical damping and matrix-free implementation, the PT method can efficiently solve large 3-D non-linear geoscience problems (Duretz *et al.* 2019; Räss *et al.* 2019).

Here in this section, we will describe how the PT solver can be developed based on physical intuition. We first analyse the general linear damped wave and identified the best damping parameter for both single and double damped wave equations. These two sets of equations involve the field evolution through physical time. We then demonstrate how to derive the PT solver with a damping scheme for a simplified system of the two-phase flow equations that ignores the shear stress, by using the physics of damped waves. This set of equation involves no physical time evolution, but pseudo-time evolution is added to solve the system. We finally couple our damping scheme with the existing damping method for the Stokes equation and form an efficient PT method for the full equations.

3.1 Single damped wave equation

For simplicity, we first consider the propagation of the 1-D damped linear wave described by the following first-order hyperbolic system:

$$\begin{cases} \beta \frac{\partial P}{\partial t} = \frac{\partial V}{\partial x} \\ \frac{\partial V}{\partial t} = \frac{1}{\rho} \frac{\partial P}{\partial x} - \frac{V}{\tau_d} \end{cases} \quad (8)$$

where P is the pressure, V is the velocity, β is the compressibility (the bulk modulus is $K = 1/\beta$), ρ is the density and τ_d is the damping parameter. Note that elastic deformation is considered here for wave propagation. This system of equations can be reduced to a single second-order wave equation:

$$\frac{\partial^2 V}{\partial t^2} = \frac{1}{\rho\beta} \frac{\partial^2 V}{\partial x^2} - \frac{1}{\tau_d} \frac{\partial V}{\partial t}. \quad (9)$$

From which it becomes clear that the solution of eq. (8) corresponds to waves propagation if $\tau_d \gg 1$ and to the diffusion process for $\tau_d \ll 1$. Let us find the optimal parameter τ_d that leads to the fastest decay of the velocity field V . The discrete version of the equation system (8) can be written as:

$$\begin{cases} \beta \frac{P_i^{l+1/2} - P_i^{l-1/2}}{\Delta t} = \frac{V_{i+1/2}^l - V_{i-1/2}^l}{\Delta x} \\ \frac{V_{i+1/2}^{l+1} - V_{i+1/2}^l}{\Delta t} = \frac{1}{\rho} \frac{P_{i+1}^{l+1/2} - P_i^{l+1/2}}{\Delta x} - \frac{1}{\tau_d} V_{i+1/2}^{l+1}. \end{cases} \quad (10)$$

Here we use a conservative staggered space-time grid discretization. The pressure P is defined at the centre of a grid cell i , and the velocity V is defined at the side of a grid cell ($i \pm 1/2$), which can be considered as a ‘flux’ through the grid cell. The temporal discretization of P corresponds to the half-integer nodes ($l + 1/2$), and the temporal discretization of V corresponds to the node integer

l . The von Neumann stability analysis for this scheme suggests (Alkhimenkov *et al.* 2021):

$$\Delta t \leq \Delta x \frac{\rho\beta\Delta x + \sqrt{(\rho\beta\Delta x)^2 + 16\rho\beta\tau_d^2}}{4\tau_d}. \quad (11)$$

A more restrictive condition is: $\Delta t \leq \Delta x/V_p$, where $V_p = \sqrt{\frac{1}{\rho\beta}}$. According to Fourier analysis, the solution of eq. (9) can be represented in the form:

$$W(x, t) = \sum_{k=1}^{\infty} Q_k e^{-\lambda_k t} \sin\left(\frac{k\pi x}{L}\right), \quad (12)$$

where t is time, x is the spatial coordinate, k is the wavenumber, Q_k is the initial amplitude of the waves at wave number k and λ_k is the eigenvalue or decay constant. Term L is the 1-D domain length. The solution of eq. (9) is thus represented by an assembly of exponentially decaying sine waves with different wavelengths. Continuous dispersion analysis of a system with the solution in the form of eq. (12) leads to:

$$\lambda_k^2 + \frac{1}{\tau_d} \lambda_k + \frac{k^2\pi^2}{\rho\beta L^2} = 0. \quad (13)$$

This shows that the decay constant λ_k for anomalies with different wavelengths depends on the choice of damping parameter τ_d . Using the standard formula for the general quadratic equation ($a\lambda^2 + b\lambda + c = 0$) gives the root of eq. (13):

$$\lambda_{1,2} = \frac{-b \pm \sqrt{b^2 - 4ac}}{2a}, \quad a = 1, \quad b = \frac{1}{\tau_d}, \quad c = \frac{k^2\pi^2}{\rho\beta L^2}. \quad (14)$$

With the solution of decay constant λ , we can next plot the decay rate for each iteration ($e^{-\lambda\Delta t}$) as a function of wavenumbers (k) and damping parameters $\Delta t/\tau_d$ (Fig. 1a). Fig. 1(a) shows that $k = 1$ has the worst decay rate among all wavenumbers, suggesting the optimal damping parameter should be chosen based on $k = 1$. A comparison of the numerical solution of eq. (10) with the analytical solution at $k = 1$ for different damping parameters shows that the necessary iteration times to achieve an accuracy of 10^{-12} perfectly matches with the analytical solution of the exponential decay process (Fig. 1b). The fastest decay rate is achieved when two roots of eq. (13) are equal (i.e. $b^2 - 4ac = 0$), leading to optimal damping parameters: $\tau_d = \frac{L}{2\pi k V_p}$ or $d = \Delta t/\tau_d = \frac{2\pi k}{n_x}$, where n_x is the number of cells in the x -direction).

3.2 The double damped wave equation

We next consider a 1-D scalar double damped linear wave propagation described by the following first-order hyperbolic system:

$$\begin{cases} \beta \frac{\partial P}{\partial t} = \frac{\partial V}{\partial x} - \frac{1}{\eta} P \\ \rho \frac{\partial V}{\partial t} = \frac{\partial P}{\partial x} - \frac{V}{k_{\eta f}} \end{cases} \quad (15)$$

This corresponds to the 2nd order partial differential equation for a damped wave of the form:

$$\rho\beta \frac{\partial^2 P}{\partial t^2} = \frac{\partial^2 P}{\partial x^2} - \left(\frac{\beta}{k_{\eta f}} + \frac{\rho}{\eta} \right) \frac{\partial P}{\partial t} - \frac{1}{\eta k_{\eta f}} P. \quad (16)$$

Versus a simple acoustic wave equation, this system has two damping terms ($\frac{1}{\eta} P$ and $\frac{V}{k_{\eta f}}$) that can have physical meaning in two-phase flow equations. Thus, the task is to choose an optimal

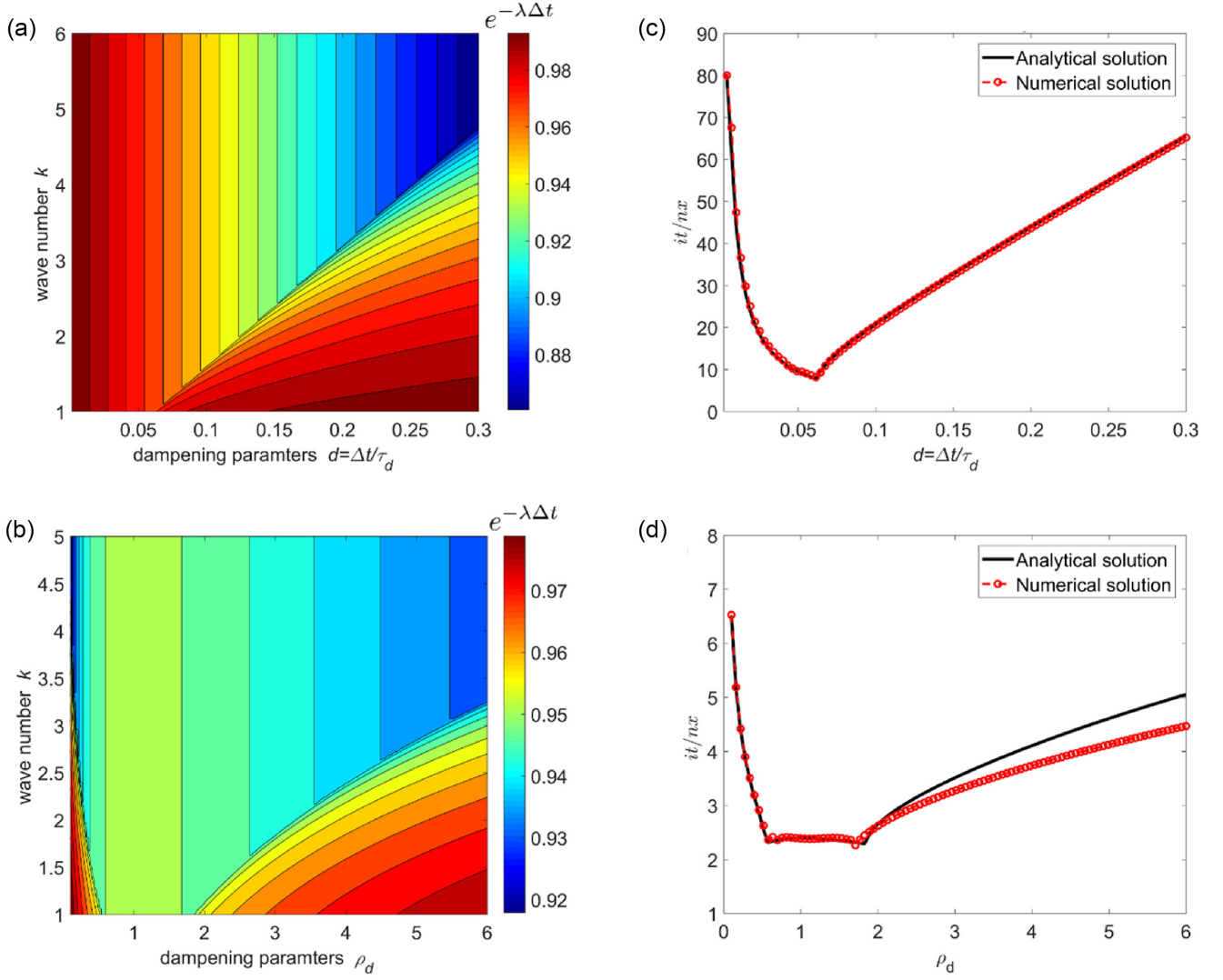


Figure 1. (a and b) The decay rate for residuals with different wavenumbers corresponding to different damping parameters for single (a) and double (b) damped wave equations. A total cell number of 100 is used for both cases. A larger absolute value of the decay rate ($\lambda\Delta t$) implies a faster the convergence process. (c and d). A comparison of the numerical and analytical processes via different damping parameters for single (c) and double (d) damped wave equations. An accuracy of 10^{-12} is used for both cases in terms of convergence criteria.

ρ and β to have the fastest decay rate, instead of η and k_{η_f} . The discrete version of this system can be written as:

$$\begin{cases} \beta \frac{P_i^{l+1/2} - P_i^{l-1/2}}{\Delta t} = \frac{V_{i+1/2}^l - V_{i-1/2}^l}{\Delta x} - \frac{1}{\eta} P_i^{l+1/2} \\ \rho \frac{V_{i+1/2}^{l+1} - V_{i+1/2}^l}{\Delta t} = \frac{P_{i+1}^{l+1/2} - P_i^{l+1/2}}{\Delta x} - \frac{1}{k_{\eta_f}} V_{i+1/2}^{l+1}. \end{cases} \quad (17)$$

The continuous dispersion analysis of eq. (15) leads to:

$$\rho\beta\lambda^2 + \left(\frac{\beta}{k_{\eta_f}} + \frac{\rho}{\eta}\right)\lambda + \frac{\pi^2 k^2}{L^2} + \frac{1}{\eta k_{\eta_f}} = 0. \quad (18)$$

With $\rho = \rho_d \beta \eta / k_{\eta_f}$, $\delta_c = \sqrt{\eta k_{\eta_f}}$ and $L = L_\delta \delta_c$, eq. (18) can be further simplified to:

$$\rho_d \eta^2 \beta^2 \lambda^2 + (1 + \rho_d) \eta \beta \lambda + \frac{\pi^2 k^2}{L_\delta^2} + 1 = 0. \quad (19)$$

Again, by using the standard formula for the general quadratic equation ($a\lambda^2 + b\lambda + c = 0$), the roots of eq. (19) are:

$$\begin{aligned} \lambda_{1,2} &= \frac{-b \pm \sqrt{b^2 - 4ac}}{2a}, \quad a = \rho_d \eta^2 \beta^2, \quad b = (1 + \rho_d) \eta \beta, \\ c &= \frac{\pi^2 k^2}{L_\delta^2} + 1. \end{aligned} \quad (20)$$

Similar to the case for the single damped wave, the system eq. (15) has the fastest decay rate ($e^{-\lambda\Delta t}$) when two roots of eq. (19) are equal (i.e. $b^2 - 4ac = 0$). Thus, the optimal damping parameters are as follows:

$$\rho = \rho_d \beta \eta / k_{\eta_f}; \quad \rho_d = \frac{2 + d \pm \sqrt{d^2 + 4d}}{2}; \quad d = \frac{4\pi^2 k^2}{L_\delta^2}. \quad (21)$$

Notice that $\delta_c = \sqrt{\eta k_{\eta_f}}$ corresponds to the compaction length in eq. (7) and L_δ is the non-dimensional length of the system. Thus, the optimal damping parameters depend on both the size of the domain and material properties.

3.3 Simple compaction-driven fluid flow equations

To illustrate the application of the PT method to two-phase models, we begin with a simplified set of equations that includes a hydraulic equation and a viscous bulk rheology in the following form:

$$\nabla_i \left(\frac{k}{\eta_f} (\nabla_i P_e + g_i \Delta \rho (1 - \phi)) \right) = \frac{P_e - P_d}{(1 - \phi) \eta_\phi}$$

$$\nabla_i q_i^D = \frac{P_e - P_d}{(1 - \phi) \eta_\phi}, \quad (22)$$

where $\Delta \rho = \rho_s - \rho_f$. These equations follow from the general model eqs (1)–(4) (Connolly & Podladchikov 2000, 2007; Yarushina & Podladchikov 2015) under the assumption that the effect of shear stresses on compaction and fluid flow is negligible and $\nabla_i \bar{P} = -\rho_i g_i = -g_i(\rho_s(1 - \phi) + \rho_f \phi)$. In fact, the first equation in (22) has one unknown (P_e) and can be solved independently, based on known porosity and permeability fields. The simplest porosity wave evolution equations are given by combining eq. (22) with eq. (6).

To apply the PT method, we rewrite eq. (22) into another form that resembles the double damped wave equation (eq. 15), which leads to:

$$0 = \nabla_i q_i^D - \frac{P_e - P_d}{(1 - \phi) \eta_\phi}$$

$$0 = \left(\frac{k}{\eta_f} (\nabla_i P_e + g_i \Delta \rho (1 - \phi)) - q_i^D \right), \quad (23)$$

where the unknown P_e and q_i^D are coupled together. We can recover the double damped wave equation (eq. 15) from eq. (23) by adding pseudo time derivatives in the left-hand sides. This means that the damping scheme in eq. (17) can be applied directly to solve eq. (23) by updating P_e and q_i^D through pseudo time.

There is more than one damping scheme for every set of equations. Here we derive another numerical damping formulation to show the PT method's diversity and variability. We rewrite eq. (23) as follows:

$$f_{P_e} = \beta_n \frac{\partial P_e}{\partial \tau} = \nabla_i q_i^D - \frac{d_1 (P_e - P_d)}{(1 - \phi) \eta_\phi}$$

$$f_{q_i} = \rho_n \frac{\partial q_i^D}{\partial \tau} = \left(\frac{k}{\eta_f} (\nabla_i P_e + g_i \Delta \rho (1 - \phi)) - d_2 q_i^D \right). \quad (24)$$

This step adds a transient time derivative to the left-hand side and damping factors d_1 and d_2 to the right-hand side. Here, ρ_n and β_n are numerical density and compressibility, respectively. Similar to pseudo time (τ), these parameters exist only for numerical reasons and have no physical meaning for the two-phase system. Understanding pseudo physical space is essential for using the numerical damping scheme and developing specific techniques for it. The goal is to solve the equation for effective pressure P_e using pseudo time-stepping, so that both P_e and q_i^D become stable when $\tau \rightarrow \infty$. The damping parameters are added to attenuate the wave energy during propagation, which significantly speeds up the convergence (e.g. Frankel 1950; Räss *et al.* 2019). Eq. (24) can be written as one equation for P_e , which has the format of a non-linear damped wave (see Appendix B). The condition that eq. (24) has the same P_e solution with eq. (23) is: $d_1 d_2 = 1$. However, adding d_1 and d_2 changed the q_i^D solution during the pseudo time-stepping when $d_1 \neq 1$, which needs to be corrected as $q_i^D = q_i^D / d_1$ for the true Darcy flux. Similar analysis with the single and double damped wave equation (Appendix B) indicates that the applicable damping

parameters are:

$$\beta_n = \frac{1}{(1 - \phi_0) \eta_c}$$

$$\rho_n = \frac{\eta_f (1 - \phi_0)}{k_0}$$

$$d_1 = -\frac{1}{2} \rho_n + \frac{\sqrt{1 + 4\rho_n}}{2\rho_n}$$

$$d_2 = \frac{1}{d_1}. \quad (25)$$

These values are calculated with the background values of ϕ_0 and η_c . According to the theory of the acoustic wave, the wave speed is:

$$V_p = \sqrt{\frac{1}{\beta_n \rho_n}} = \sqrt{\frac{k_0 \eta_c}{\eta_f}}. \quad (26)$$

This has a similar format of the compaction length (eq. 6), suggesting that the speed of the damped wave in pseudo physical space equals the compaction length that depends on the permeability, bulk viscosity and fluid viscosity. As the permeability and bulk viscosity vary in space, the wave speed of the damped wave varies in space accordingly. As we find, applying a local value of V_p for each node in the pseudo-time stepping significantly accelerate the convergence. Its effect is analogous to a diagonal pre-conditioner for matrix-based solvers (Duretz *et al.* 2019; Räss *et al.* 2019). Thus, the pseudo-time stepping is:

$$\Delta \tau_{P_e} = \frac{1}{X_d} \frac{\min(\Delta x_i)}{n_{\text{dim}} V_p}$$

$$q_i^k = q_i^{k-1} + \Delta \tau_{P_e} f_{q_i^k} / \rho_n$$

$$P_e^k = P_e^{k-1} + \Delta \tau_{P_e} f_{P_e^k} / \beta_n, \quad (27)$$

where Δx_i is the cell size in the i directions ($i = z$ in 1-D, x, z in 2-D, x, y, z in 3-D), and n_{dim} is the spatial dimension (1, 2, 3). We replace q_i^D with q_i . Local values of ρ_n , β_n and V_p are applied in eq. (24) to speed up the convergence. Applying these techniques based on physical intuition leads to a robust algorithm of the pseudo-transient solver. The required iteration number scales linearly with numerical resolution in one direction (e.g. n_z node number in the z -direction).

3.4 Full two-phase flow equations

Now we will apply the same technique to derive the pseudo-transient solver for the full set of governing equations. By adding a transient time derivative to the force balance eq. (1) and the constitutive eq. (4), the full equations of the two-phase flow can be written as:

$$f_{v_i} = \frac{\partial v_i}{\partial \tau_{v_i}} = \nabla_j (\bar{\tau}_{ij} - \bar{P} \delta_{ij}) - g_i \bar{\rho}$$

$$f_{\bar{P}} = \frac{\partial \bar{P}}{\partial \tau_{\bar{P}}} = -\nabla_k V_k - \frac{P_e - P_d}{(1 - \phi) \eta_\phi}$$

$$f_{(P_e)} = \beta_n \frac{\partial P_e}{\partial \tau_{(P_e)}} = \nabla_i q_i^D - \frac{d_1 (P_e - P_d)}{(1 - \phi) \eta_\phi}$$

$$f_{q_i} = \rho_n \frac{\partial q_i^D}{\partial \tau_{q_i}} = \frac{k}{\eta_f} (\nabla_i P_e - \nabla_i \bar{P} - g_i \rho_f) - d_2 q_i^D. \quad (28)$$

For the shear stress, we introduce a numerical bulk viscosity (η_b) to update it with the pseudo-transient stepping:

$$\bar{\tau}_{ij} = 2\mu_s \left(\frac{1}{2} (\nabla_i v_j + \nabla_j v_i) - \delta_{ij} \left(\frac{1}{3} \nabla_k v_k + \eta_b f_{\bar{P}} \right) \right), \quad (29)$$

where f_{v_i} , $f_{\bar{P}}$, f_{P_e} , f_{q_i} are the residuals, which will approach zero during pseudo-transient time-stepping. Note that eq. (29) introduces a numerical term ($\eta_b f_{\bar{P}}$) in the shear stress update, but its effect on shear stress disappears when $f_{\bar{P}}$ approaches zero. As we find, it is useful to adjust η_b when the ratio of shear viscosity and bulk viscosity changes.

The pseudo-time steps for velocity V_i and pressure \bar{P} are (Duret *et al.* 2019; Räss *et al.* 2019):

$$\begin{aligned}\Delta\tau_{v_i} &= \frac{1}{X_v} \frac{\min(\Delta x_i)^2}{2.1n_{\text{dim}}\mu_s(1+\eta_b)} \\ \Delta\tau_{\bar{P}} &= \frac{1}{X_p} \frac{2.1n_{\text{dim}}\mu_s(1+\eta_b)}{\max(n_i)},\end{aligned}\quad (30)$$

where Δx_i and n_i are the cell size and number of cells in the i direction ($i = z$ in 1-D, x, z in 2-D, x, y, z in 3-D); η_b is a constant for an analogy of numerical bulk viscosity. Similar to V_p , the local value of μ_s can be applied in eq. (30) when the shear viscosity varies in space, as shown in Section 4.2.3, where we consider models with multiple layers of different physical properties.

The pseudo time-stepping that approach the solution through iteration for the momentum and mass equations (including stress update) are:

$$\begin{aligned}v_i^k &= v_i^{k-1} + \Delta\tau_{v_i} g_{v_i}^k \\ g_{v_i}^k &= f_{v_i}^k + \left(1 - \frac{V_n}{n_i}\right) g_{v_i}^{k-1} \\ \bar{P}^k &= \bar{P}^{k-1} + \Delta\tau_{\bar{P}} f_{\bar{P}}^k \\ \bar{\tau}_{ij}^k &= 2\mu_s \left(\frac{1}{2} (\nabla_i v_j^k + \nabla_j v_i^k) - \delta_{ij} \left(\frac{1}{3} \nabla_i v_i^k + \eta_b f_{\bar{P}}^k \right) \right).\end{aligned}\quad (31)$$

Note that damping is applied to the residual of the momentum equation (f_i), for which a fraction of the previous update (g^{k-1}) is added to the current residual (f^k) for the velocity update. This is different from the direct damping of the effective pressure field (P_e) in eq. (27), and it can also speed up the convergence. We found that $V_n = \pi$ leads to optimal convergence and that there is no need to apply damping for the total pressure when damping is already applied to the field of effective pressure and velocity.

Thus, the pseudo-transient continuation with damping schemes for the full equations are given through a combination of eqs (28–31). PT stepping is performed until the residual for each equation ($f_{v_i}^k$, $f_{\bar{P}}^k$, $f_{P_e}^k$, $f_{q_i}^k$) becomes small enough, that is $\|f\| < \varepsilon$. Just as the equations couple each other to form full equations for the two-phase system, the pseudo-transient formulations can also couple together and form numerical schemes for the full equations. As we found, the residual of every equation decays exponentially similar to when they are solved independently. That is, just as the equations can be coupled physically, the numerical damping schemes can also be coupled to solve them.

4 NUMERICAL EXAMPLES

This section shows numerical examples and the convergence results of our PT solver for models with different rock properties. We consider two different model setups corresponding to either a fluid-filled reservoir overlain by rock layers with lower porosity (Figs 2a and b) or a higher-porosity inclusion-like domain in the otherwise homogeneous rock (Fig. 2c). The porosity of the reservoir is initialized as $\phi_r = \phi_0(1 + \phi_A)$, where ϕ_0 is the background porosity, and ϕ_A is the porosity contrast. The porosity contrast $\phi_A = 3$ in Figs 2(a) and (b) and is $\phi_A = 2$ in Fig. 2(c). The corresponding

numerical results for Fig. 2 are presented in Figs 3, 5 and 9. Initial conditions for our other models are similar to Fig. 2 and are plotted with the models' results. The boundary conditions indicated in Fig. 2(c) apply to all 2-D models.

To study fluid flow in different geological environments, we explore a wide range of parameters in our 1-D and 2-D models. We first solve the simplified equations that ignore the influence of shear stresses for 1-D and 2-D models. The effects of background porosity (ϕ_0), decompaction weakening factor (R), porosity contrast (ϕ_A), permeability exponent (n_p) and the topography of the initial reservoir are explored. These simplified models help explain fluid flow in deformable porous rocks. We then solve the full equations that include shear stresses. In addition to previous parameters, we investigate the role of the ratio between bulk and shear viscosities, rheology (bi-linear versus viscoplastic), the geometry of the system, and rock heterogeneity presented via a layered structure for permeability and bulk viscosity. These models can be applied to more realistic situations where stratified geological layers exist. Finally, we show the numerical convergence of our PT solver for models with different parameters.

4.1 Simple compaction-driven fluid flow

4.1.1 1-D porosity wave

In 1-D simulations, we first study how the elongated fluid channels develop from a high porosity reservoir in rocks with decompaction weakening using viscous bilinear rheology. The porosity in the reservoir is three times higher than the background value (i.e. $\phi_A = 3$). The simulation results for three different background porosities ($\phi_0 = 0.001$, $\phi_0 = 0.01$, $\phi_0 = 0.1$) are presented in Figs 3(a)–(c). They show that the porosity within the reservoir decreases to the background value ϕ_0 over time. Porosity distribution within the entire domain acquires a sharp Gaussian gradient. The porosity profiles elongate in the propagation direction (vertically upward) in all three models, leaving a slightly higher porosity when the wave peaks pass. The maximum porosity in each model is maintained through time. The two models with small background porosities ($\phi_0 = 0.001$, $\phi_0 = 0.01$) show quite similar evolutions as the wave fronts propagate from $z = 5$ to 15 after one compaction time, δ_t , (orange lines in Figs 3a and b). The propagation in model with $\phi_0 = 0.1$ is noticeably slower (Fig. 3c).

We then vary the decompaction weakening factor R , porosity contrast (ϕ_A) and permeability exponent (n_p) independently, based on the model with a background porosity $\phi_0 = 0.01$. Figs 3d–e) shows the porosity profiles at $t = \delta_t$ for models with different R and ϕ_A . Fig. 3(f) shows profiles at $t = 0.5 \delta_t$ for models with different n_p . Without decompaction weakening ($R = 1$), the fluid accumulates and forms a localized domain with much higher porosity (up to $\phi_{\text{max}} = 0.07$) than incases with $R \gg 1$. However, upward migration of this high porosity domain is very slow. With decompaction weakening ($R = 10$ –1000), fluid accumulation is significantly reduced and the porosity profile elongates (Fig. 3d). The wavefront moves faster and becomes shaper with increasing R . The effects of porosity contrast (ϕ_A) is shown in Fig. 3e). With increasing ϕ_A , the maximum porosity developed by the porosity wave increases and the wave fronts propagate faster. Large contrasts in porosity generally lead to much faster and larger porosity waves. Fig. 3(f) shows the effects of the permeability exponent n_p on the porosity wave: The wavefront propagates faster at higher values of n_p . The speed of propagation for $n_p = 5$ is about three times the speed for $n_p = 3$

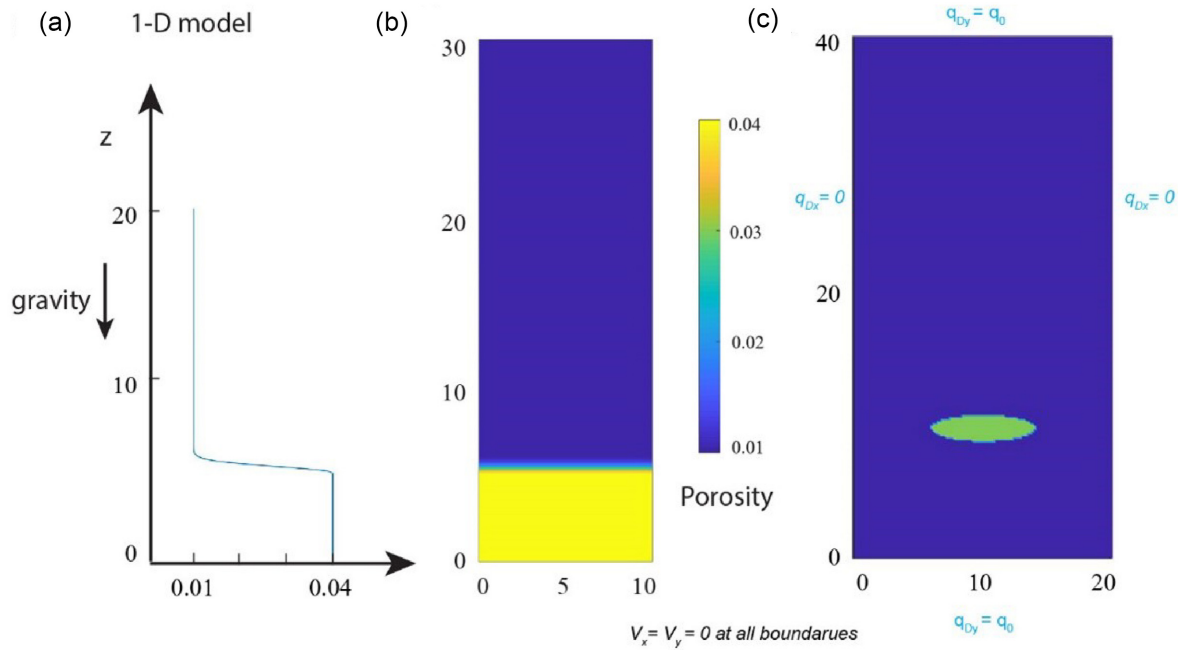


Figure 2. (a) Initial porosity profile for 1-D models with background porosity $\phi_0 = 0.01$; (b) initial porosity field for 2-D models with a high-porosity reservoir (i.e. Section 4.2.1) and (c) initial porosity field and boundary conditions for models with an elliptical inclusion of higher porosity (i.e. Section 4.2.4). A Gaussian gradient is applied to the porosity profiles for both 1-D models (a) and 2-D models with a flat topography of reservoir (b).

in Fig. 3(f). Meanwhile, the maximum porosity within the porosity wave decreases slightly with increasing n_p .

4.1.1 2-D porosity wave

To study the effect of reservoir topography on the development/initiation of localized fluid channels, we test the effects of different curvatures of the reservoir top in 2-D models. The following ellipse defines the reservoir curvature:

$$\left(\frac{x-5}{x_a}\right)^2 + \frac{(y-2)^2}{16} = 1.$$

Three different values of x_a (8, 16, 32) are used in our simulations (Figs 4a–c). Higher values of x_a lead to a flatter reservoir topography. Another model with a completely flat reservoir boundary is presented for comparison in Fig. 4(d). For $x_a = 8$, all fluids feed into one main channel in the middle. For $x_a = 16$, two large channels form in the middle and two small channels form at the sides. For $x_a = 32$, two large channels form at the sides and one small channel forms in the middle. With a completely flat topography, channel formation is significantly delayed with no localized channels observed at $t = 0.5 \delta_r$; two channels start to form at $t = 0.9 \delta_r$. These results suggest that the localized fluid channels, ignited by the topographic variations in the reservoir, are the natural outcome of flow instability in the system.

4.2 Full two-phase flow

4.2.1 Conditions for developing fluid channels/flow instability

We next present numerical solutions for the full set of equations described in Section 2.1, accounting for shear stresses as well as the

pressure load. Previous studies have shown that the flow instability that forms flow channels develops only under special conditions. These might be met in situations when the fluid flux is too high to be accommodated by a pore space without deformation, or when sedimentation is too rapid versus background Darcy's flow rate (Audet *et al.* 2009; Yarushina & Podladchikov 2015). The results from the previous section also show that slow upward propagation of a stable fluid front is an alternative to the fluid flow focusing into separate channels (Fig. 4d). Here, we investigate the conditions at which the fluid channels develop from a stable/flat front. For that, we calculated models with different background porosities ϕ_0 and shear viscosity (by varying C), assuming a flat reservoir topography (Fig. 5). By varying C , we also change the ratio between shear viscosity and bulk viscosity ($\frac{\mu_s}{\eta_c} = \frac{\phi_0^0}{C}$), which is an important indicator.

For models with $C = 1$ (Figs 5a–c), only model with $\phi_0 = 0.001$ develops localized fluid channels before the stable flat fluid front reaches the top. Upon comparing the models in Fig. 5(d) ($C = 0.1$) and Fig. 5(a) ($C = 1$), we can see that localized fluid channels do not form when the shear viscosity is increased by 10 times for models with background porosity $\phi_0 = 0.001$. Upon comparing the models in Fig. 5e ($C = 10$) and Fig. 5b ($C = 1$), we see that fluid channels start to form when the shear viscosity is reduced by 10-fold for models with background porosity $\phi_0 = 0.01$. Similarly, fluid channels forms when the shear viscosity is low ($C = 100$ in Fig. 5f) but do not form when the shear viscosity is high ($C = 1$ in Fig. 5c) for models with $\phi_0 = 0.1$. While both background porosity ϕ_0 and C matter, it is the viscosity ratio $\frac{\mu_s}{\eta_c} = \frac{\phi_0^0}{C}$ that ultimately determines whether the fluid channels form or not in these models. In general, low viscosity ratios promote channel formation, while large viscosity ratios inhibit the formation of channels. A viscosity ratio of 10^{-3} is required for the fast development of localized fluid channels with $n_p = 3$ from a flat reservoir.

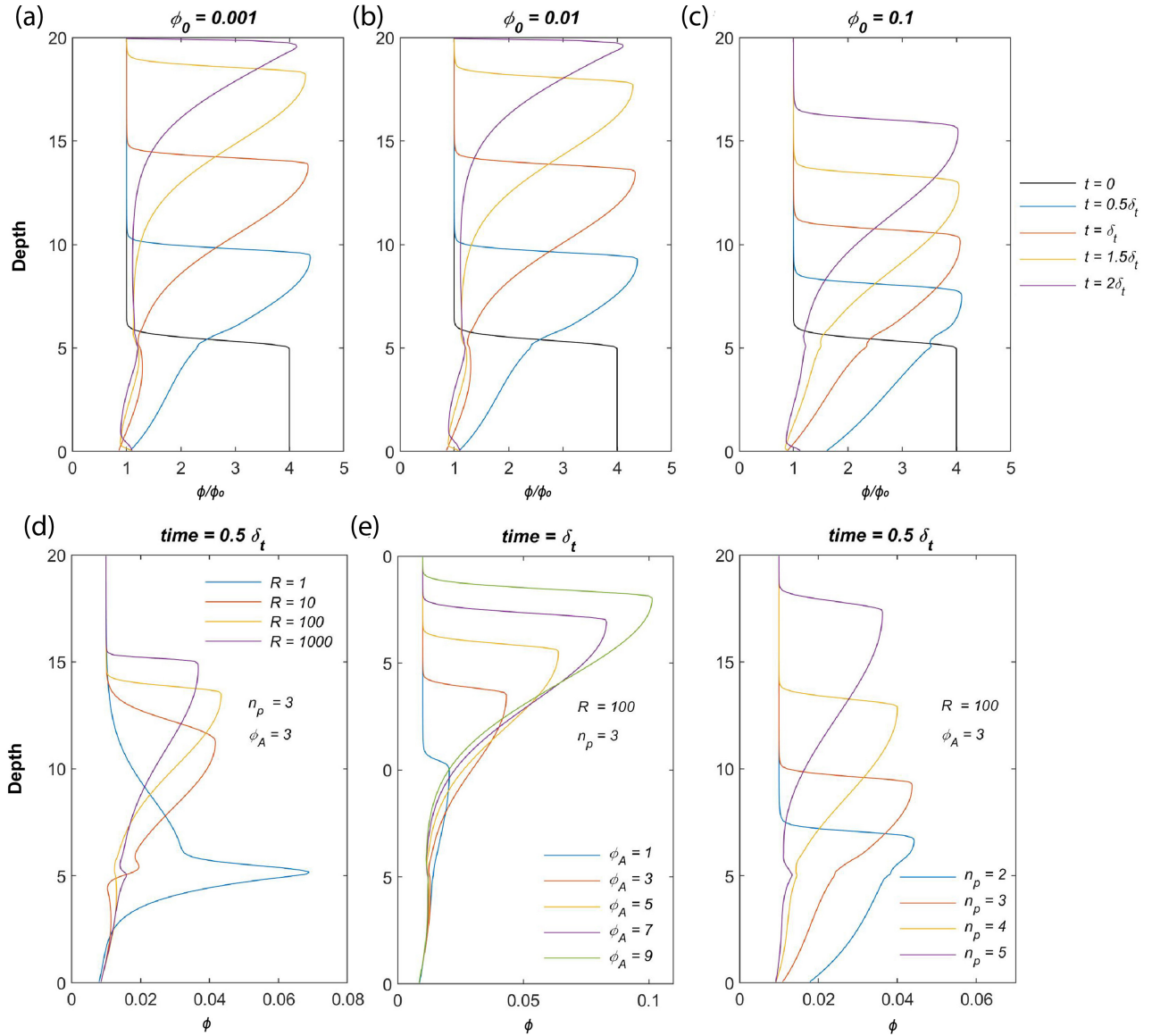


Figure 3. 1-D porosity wave in the simple compaction-driven flow system. (a–c) Time evolution of porosity wave at different background porosity $\phi_0 = 0.001$ (a); $\phi_0 = 0.01$ (b); $\phi_0 = 0.1$ (c). (e–f) Influence of the decompaction weakening factor R (d), porosity contrast ϕ_A (e), and permeability exponent n_p (f) on the propagation of porosity wave. The decompaction weakening elongates the wave in the propagation direction. The porosity contrast ϕ_A and permeability exponent n_p control the amplitude and speed of the waves.

4.2.2 Reservoir with surface relief

In Section 4.1.2, we saw that the curvature of the reservoir top affects the formation and location of fluid channels. Here we investigate how small scale reliefs of the reservoir top affects the development of localized fluid channels. These models are run with $\phi_0 = 0.1$, $n_p = 5$, $\phi_A = 2$, and $C = 100$. First, we consider models with a single bump of different widths on the otherwise flat surface and test the influence of the width (Figs 6a, c and e). These results show that when a single but wide bump is present at the reservoir top, two separate channels form in the middle of the domain flanked by two smaller channels that develop slightly later (Fig. 6a). Only one channel originates from the bump when the width of the bump is reduced by three (Fig. 6c) or six (Fig. 6e) times. This central channel is also flanked by two symmetrical channels that develop outside the bump area. We then consider models with two smaller bumps that are located at varying distances from each other (Figs 6b, d and

f). Two separate channels start to form at the two bumps that are present at the top of the reservoir. As the channels develop, however, they can merge into a single wider channel if the distance between the bumps is too small to support two channels (Fig. 6b). A bigger distance between bumps leads to larger drainage area for each of the channels to grow. Thus, two separate fluid channels develop and do not merge into one channel in the case with larger distance between the bumps (Figs 6d and f).

4.2.3 Reservoir with sinusoidal geometry

This section considers the reservoir of the same thickness but with sinusoidal topography of varying wavelengths (Fig. 7). These models are calculated with $n_p = 3$, $R = 100$, and $\phi_0 = 0.1$. Figs 7(a)–(c) show how multiple channels develop through time, starting from the

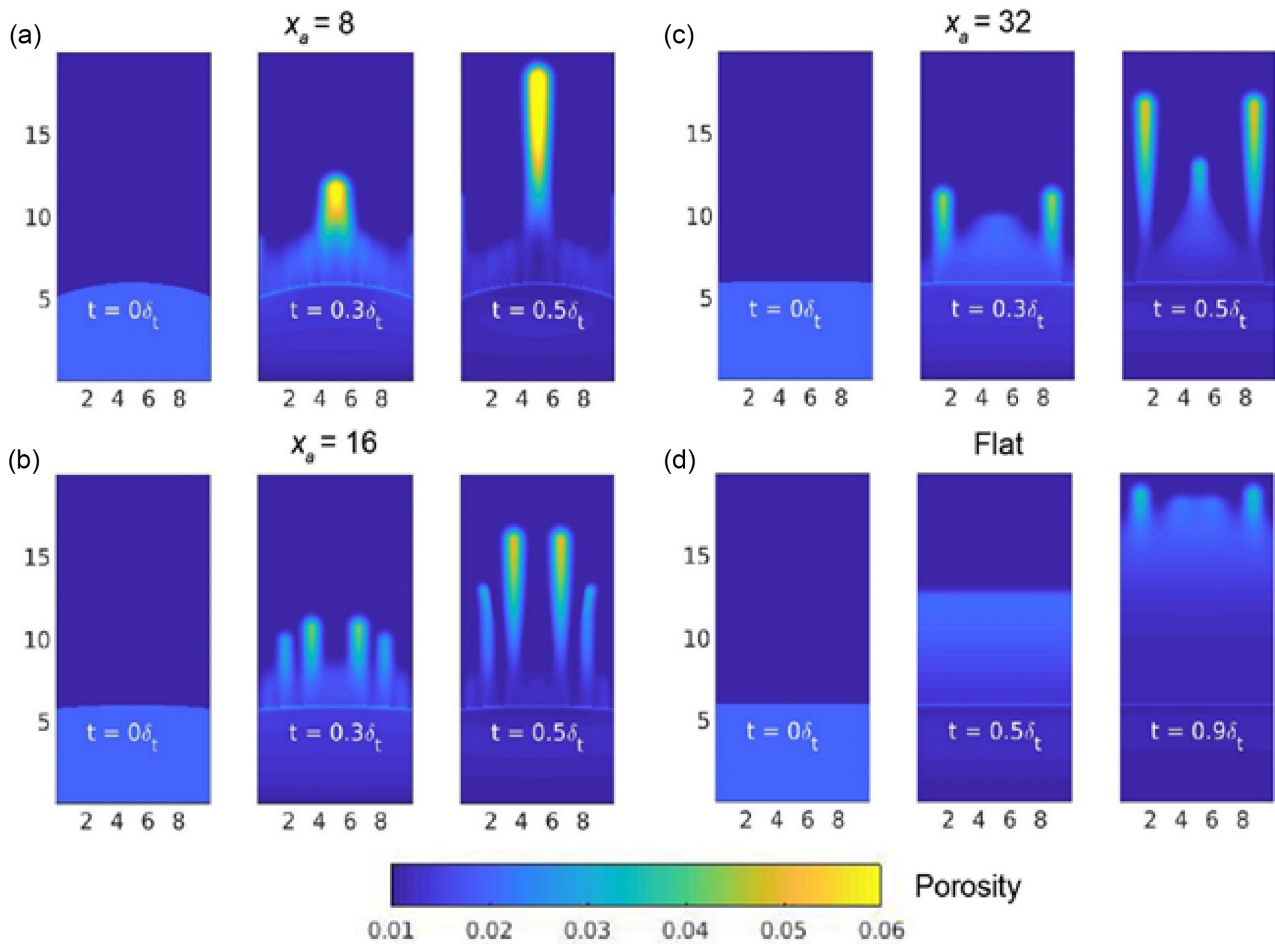


Figure 4. Formation of localized channels from reservoirs with different topography. The upper boundary of the reservoir is defined by ellipses with different curvatures: $x_a = 8$ (a), $x_a = 16$ (b), $x_a = 32$ (c) and flat ($x_a = \text{inf}$) (d). The fluid channels develop through the vertical elongation first and then horizontally focusing/narrowing. The curvature of the reservoir boundary determines where the channel forms through the flow instability in the system. Initial background porosity is: $\phi_0 = 0.01$; porosity contrast is: $\phi_A = 1$.

sinusoidal crest points (see evolution movie in the Supporting Information). The channels become wider, more diffuse and slower as the wavelength of a sine curve increases and the curvature of its elevated parts decreases (Fig. 7d). Further increase in the wavelength of sinusoidal reservoir leads to the formation of multiple smaller channels within a wavelength (Figs 7e and f). Their spacing and size are mostly controlled by the compaction length, while the location is somewhat influenced by the discretization. This can be seen from that channels tend to form in places with sharp topographic gradients, that is at the flanks of individual horizontal plateaus forming the sinus. The shear viscosity in the model in Fig. 7(f) is reduced by ten times, leading to more focused fluid channels with higher porosity than in Fig. 7(e).

To quantify how the presence of geological layers with different material properties influences fluid channel formation, we next consider a setup where a layer with different viscosities or permeabilities is placed in the overburden (Fig. 8). Variations of rock viscosity and permeability lead to changes in the compaction length and compaction time from layer to layer. Given that the channel widths are strongly affected by compaction length and the propagation time is scaled to the compaction time, one might expect that the width of the channels and the speed of propagation would also change from one layer to another. Indeed, by placing an additional layer with viscosities (both shear viscosity and bulk viscosity) that

are 10-fold the background viscosity (strong layer), we see that the channel becomes wider in the strong layer but then resumes its initial width once it reaches the rock with the background viscosity (Fig. 8a). Interestingly, some of the fluid ponds underneath the strong layer (Fig. 8a). On the contrary, the channels become narrower within the weaker layer that has 10-fold smaller viscosities. However, when the channel finally leaves the weak layer, it gains much higher porosity than the lower parts of the channel (Fig. 8b). The overall distances reached by the channels with weak and strong layers are slightly different from the models in Fig. 7(c). A strong layer delays fluid propagation, while a weak layer leads to faster fluid propagation.

Figs 8(c) and (d) show the influence of a layer with lower or higher permeability than in the background. The permeability of this layer is reduced by 10-fold and the viscosities do not change in Fig. 8(c). Thus, fluid channel growth is first arrested, and porosity within this layer starts to grow through a fluid supply from beneath. The porosity above the low-permeable layer is concurrently reduced. Fluid has enough porosity to enter the low permeability layer but does not have enough time to move through it as efficiently as before. Yet, we see that new channels start to grow within the low-permeable layer getting ready to propagate further. Note that we consider here a simplified situation when porosity and viscosity of the low-permeable layer are the same as of the surrounding

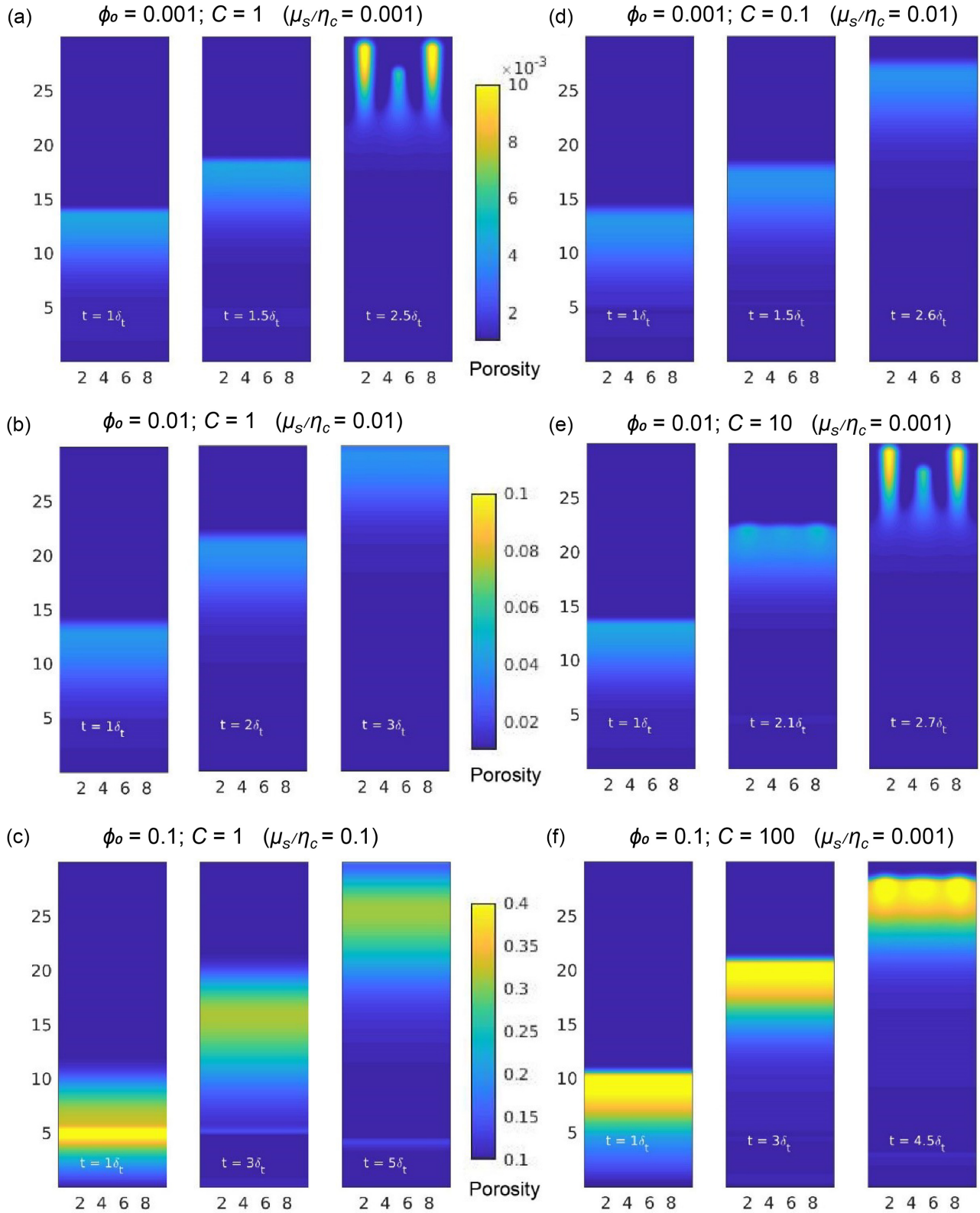


Figure 5. Localized versus pervasive fluid flow patterns that develop from a flat reservoir in two-phase models with different combinations of background porosity and parameter C . (a–c). The evolution of porosity field for models with $\phi_0 = 0.001$ (a), $\phi_0 = 0.01$ (b) and $\phi_0 = 0.1$ (c) with $C = 1$. (d–f). The evolution of porosity field for models with different background porosities and C : $\phi_0 = 0.001$, $C = 0.1$ (d), $\phi_0 = 0.01$, $C = 10$ (e), $\phi_0 = 0.1$, $C = 100$ (f). By varying parameter C , we change the shear viscosity and viscosity ratio $\frac{\mu_s}{\eta_c} = \frac{\phi_0}{C}$ in models with the same background porosity. Effective bulk viscosity η_ϕ is defined by eq. (5) with $R = 100$. No initial bump structure of the reservoir is applied to initiate the channels. Like the simplified equation experiments, the fluid channels develop through the vertical elongation first and then horizontally focusing.

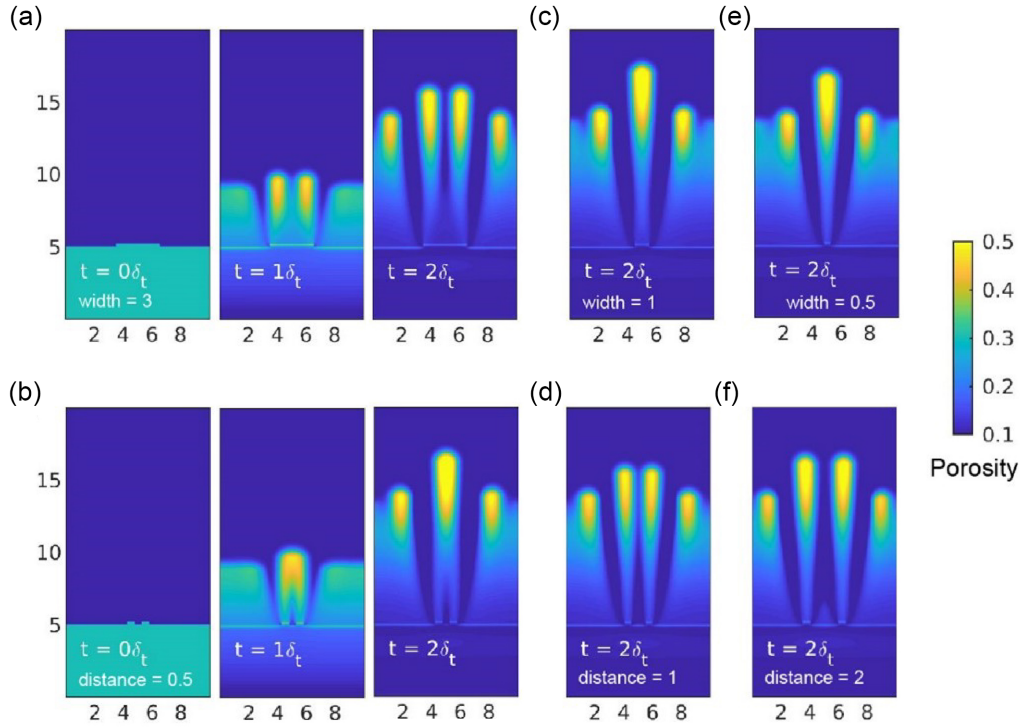


Figure 6. Development of fluid channels from reservoirs with different top surface relief (a) Single square elevation with different widths ($3\delta_c$, δ_c , $0.5\delta_c$) is imposed in the middle of the reservoir top; (b) two square elevation/bumps with width of 0.5 are imposed at the top of the reservoir at different distances ($0.5\delta_c$, $1\delta_c$, $2\delta_c$) and (c) a single square elevation of different sizes ($6\delta_c$, $0.5\delta_c$) is imposed at the top of the reservoir. Simulations are performed for $\phi_0 = 0.1$, $n_p = 5$, $\phi_A = 2$, $C = 0.01$.

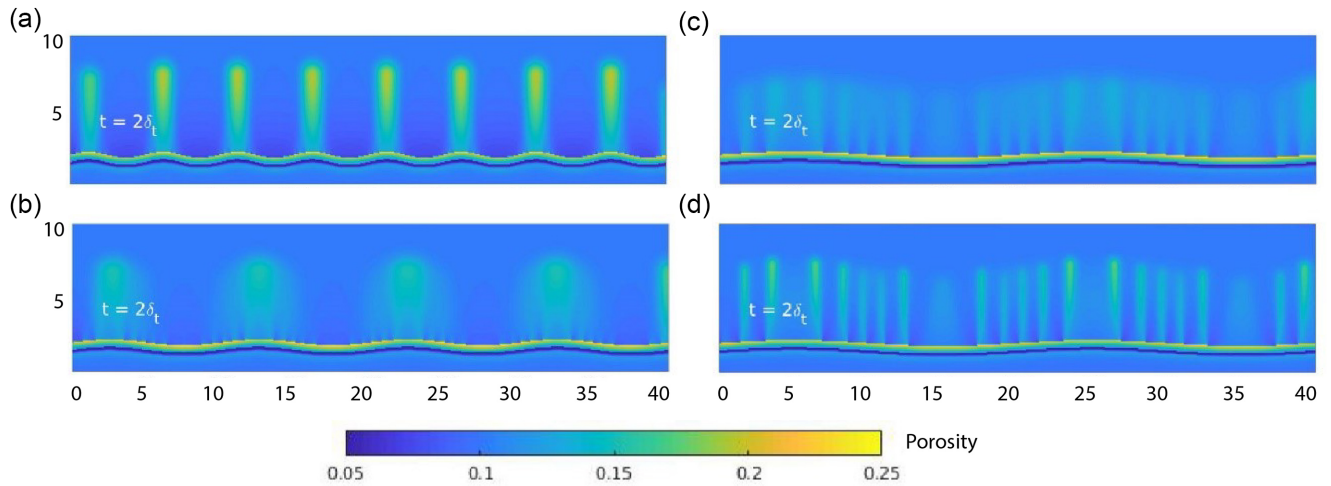


Figure 7. Fluid channels formed from sinusoidal reservoirs with different wavelengths: (a) short wavelength with a peak number of $k_w = 4$; (b) intermediate wavelength with a peak number of $k_w = 4$; (c, d) long wavelength with a peak number of $k_w = 2$. Models in (a-c) have the same shear viscosity. Model in (d) has 10-fold lower shear viscosity than other models. The background porosity is $\phi_0 = 0.1$.

rock. When modelling real geological environments, both permeability and viscosity need to be varied alongside with porosity. On the other hand, the porosity in this layer is significantly decreased when the permeability of this layer is ten times higher than the background value (Fig. 8d), including the porosity in the channels. When the channels pass through this layer and enter the layer above, the porosity increase significantly and show a higher contrast with surrounding rocks (Fig. 8d). Note that changing permeability of this layer also has a significant effect on the porosity evolution in the layer above. A less permeable layer reduces the fluid supply for the

above layer, resulting in low porosity (Fig. 8c). In contrast, a more permeable layer increases porosity in the above layer by supplying more fluid flow to it (Fig. 8d).

4.2.4 Small elliptical fluid-filled inclusion

In this section, we document the results for porosity waves that originate from a higher-porosity inclusion-like domain in the otherwise homogeneous rock (Fig. 2c). We use two types of rheology in this section: Two models have the viscous bilinear rheology with

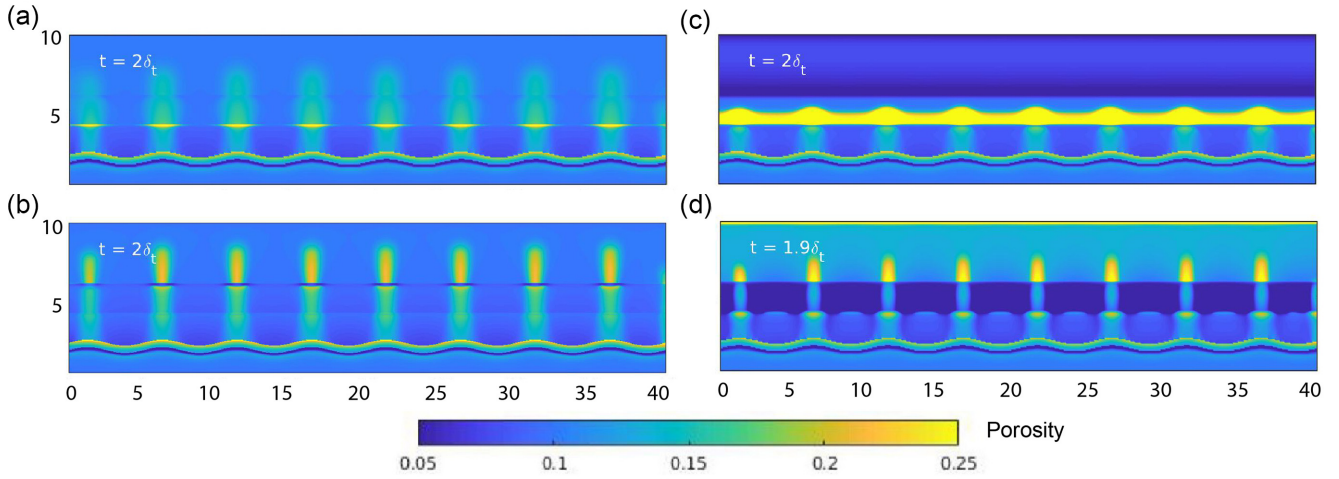


Figure 8. Development of fluid channel through four different stratified rocks. In these four models, a layer of material has been made ten times stronger (a); weaker (b); less permeable (c) and more permeable (d). This layer is present in the overburden. The reference bulk viscosity (η_c) or permeability (k_0) is changed by ten times in this layer. The model resolution is 512×128 for this set of models. A higher resolution (1024×256) is used in the model with a weaker layer for better convergence. Movies that show full evolution of these models can be found in the supplementary material.

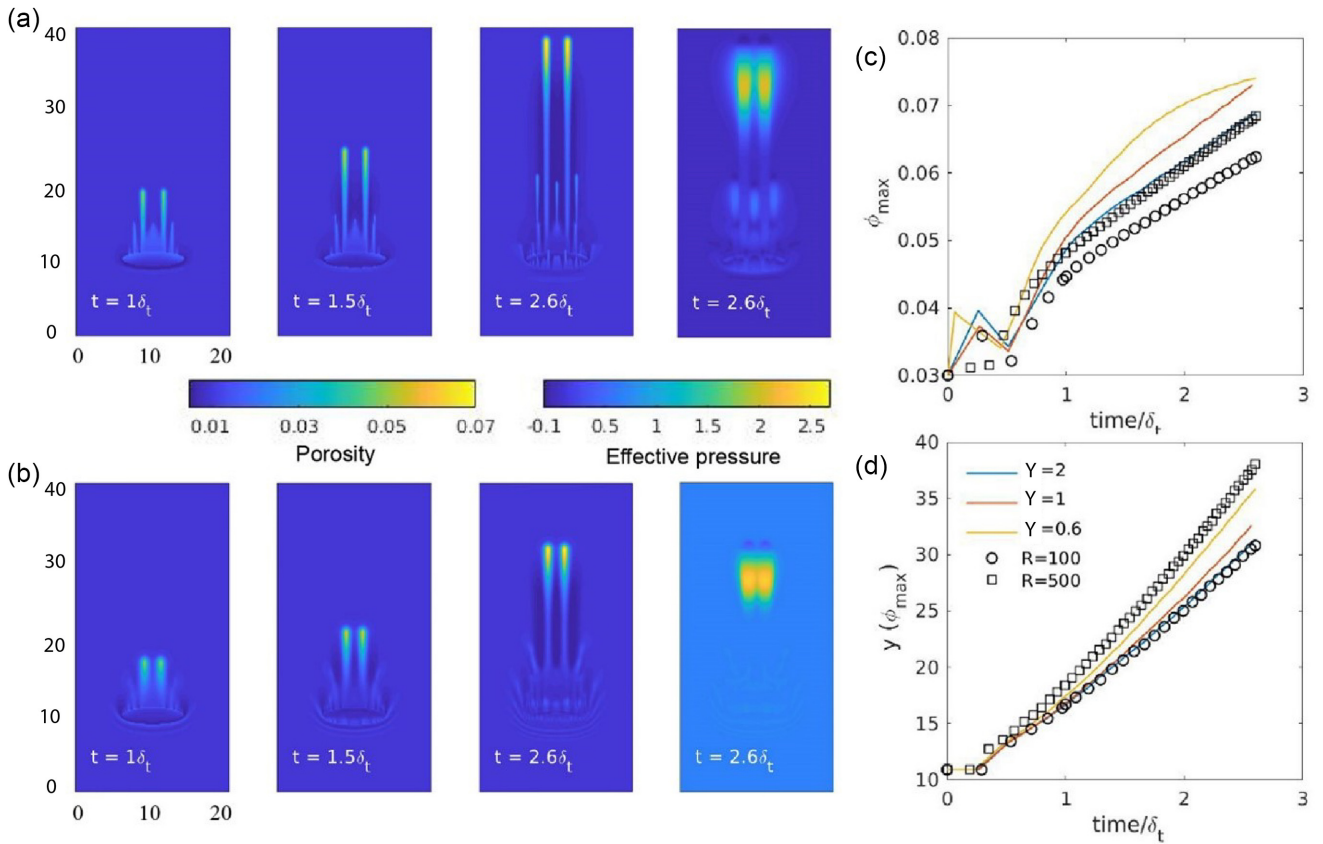


Figure 9. Effect of rock rheology on the development of fluid channels. (a) The evolution of porosity field at $t = 1\delta_t, 1.5\delta_t, 2.6\delta_t$ and effective pressure at $t = 2.6\delta_t$ (column 4) for a model with viscous bilinear rheology ($R = 500$). (b) The porosity field evolution at $t = 1\delta_t, 1.5\delta_t, 2.6\delta_t$ and effective pressure at $t = 2.6\delta_t$ (column 4) for models with viscoplastic rheology $Y = 2$. (c and d) Evolution of maximum porosity (c) and depth of max porosity (d) in five models with two types of rheology. The circle and star lines are for models with viscous bilinear rheology with R factors, while the solid lines are for models with viscoplastic rheology. In this set of models, the viscosity ratio (μ_s/η_c) is 0.001 ($C = 0.1, \phi_0 = 0.01$), while the effective pressure transition zones (λ_p) is 0.01. (Rass *et al.* 2019)

decompaction weakening factor R (100 and 500); The Other three models have the viscoplastic rheology ($Y = 2, 1, 0.6$) (Appendix A). Fig. 9(a) shows fluid channels development in rocks with viscous bilinear rheology at $R = 500$, which is a reproduction of the model with the resolution of 128×256 in fig. 5 in Rass *et al.* 2019. Fig. 9(b) shows the development of fluid channels in rocks with the viscoplastic rheology ($Y = 2$). Fluid channels produced using these two different types of rheology are very similar. However, the advantage of the viscoplastic model is that it gives more realistic predictions for the effective pressure, which is positive everywhere (Fig. 9b), compared to the negative effective pressure at the channel fronts in viscous bilinear models (Fig. 9a). It is also clear that the maximum porosity is generally larger with viscoplastic rheology than with viscous bilinear rheology (Fig. 9c). The speeds of channel development in models with the viscoplastic rheology, however, are between the speeds of the two models with decompaction weakening factor $R = 100$ and $R = 500$, as shown in Fig. 9(d).

4.2.5 Effects of different rock properties

To study the development of fluid channels with materials that have different properties, we next test the effects of permeability exponents (n_p), porosity contrast (ϕ_A) and decompaction weakening factor (R). All models consider a flat reservoir with a small bump (size of 0.5×0.5) to initiate the channel in the middle. The modelling domain is 10×30 . Fig. 10(a) shows the initial condition and evolution of porosity waves: A strong fluid channel quickly develops from the bump, and two small channels develop at its sides later. By varying the porosity contrast (ϕ_A), we can see that the main channels become stronger and wider with increasing ϕ_A . These also develop slightly faster, as shown in Fig. 10(b). With $n_p = 3$, a similar main channel develops but has a narrower width, while the widths of the channels increase significantly for models with $n_p = 10$ and $n_p = 15$, as shown in Fig. 10(c). As a matter of fact, the channel width in the model with $n_p = 15$ becomes too wide for the side channels to develop within the model domain (Fig. 10c). Another important effect of increasing n_p is that the channel propagates much faster, as indicated by each model's time label. It takes $t = 5.1\delta_t, 1.7\delta_t, 0.4\delta_t$ and $0.2\delta_t$ for models with $n_p = 3, 5, 10$ and 15 to reach nearly the top of the model domain (Figs 10a and c), respectively. The decompaction weakening R factor also plays an important role in channel development (Fig. 10d). Without decompaction weakening ($R = 1$), no channel develops even with an initial bump. A weak (low porosity) but wider fluid channel develops with $R = 10$. With $R = 1000$, the fluid channels are faster and stronger than models with $R = 10$ and $R = 100$.

The effects of different parameters can be clearly shown by plotting the evolution of statistical data, such as the maximum porosity and its locations (Fig. 11). The maximum porosity increases quickly at the beginning of all models—this growth then, the growth slows down as indicated by the slope of the line plotted in Fig. 11(a). High porosity contrast (ϕ_A) between the reservoir and the background leads to much higher maximum porosity, as shown by the dashed line (Fig. 11a). From the evolution of the location of the maximum porosity in Fig. 11(b), it is clear that the permeability exponent (n_p) plays a dominant role in the speed of channel development. The speed increases ~ 10 times from $n_p = 5$ to $n_p = 15$. A higher porosity contrast (ϕ_A) increases the speed when the permeability exponent (n_p) is fixed. The decompaction factor R also has an effect. The speed is much lower in the model with $R = 10$ than in models

with $R = 100$ and $R = 1000$. However, little change is observed when we increase R from 100 to 1000.

4.3 Numerical convergence

In this section, we demonstrate the numerical convergence of our numerical schemes with different permeability contrasts for both the simplified decoupled equations and full equations. Extra iterations are always needed for the 1st step, and thus we chose the 2nd step to show the convergence for each model with different parameters. The evolution of the minimum L2 norm among the residuals ($f_{v_i}^k, f_{\bar{p}}^k, f_{P_e}^k, f_{q_i}^k$) are plotted in Fig. 12. We run two sets of models for 1-D simplified equations: (1) $n_p = 5$ and $0.5 \leq \phi_A \leq 8$; (2) $\phi_A = 0.5$ and $3 \leq n_p \leq 20$. These models are run until the residuals reach the machine limits. The residuals converge exponentially in all models, and the convergence speed is related to the value of n_p and ϕ_A : A smaller ϕ_A or n_p leads to faster convergence (Figs 12a and b). It takes approximately n_z or $2n_z$ iterations (n_z is the cell number in the vertical direction) to converge to 10^{-5} for the commonly used n_p (e.g. 3) and ϕ_A (e.g. 0.5 or 1). The models with low and intermediate values of ϕ_A (< 3) and n_p (< 15) converge to $\sim 10^{-5}$ within $5n_z$ iterations. In fact, these calculations nearly converge to the machine precision (10^{-16}) within $15n_z$ iterations. For the full equations, the residuals also have exponential decay trends but with periodic disturbances, as shown in Figs 12(c) and (d). Versus the simplified equations, it takes more iterations for low and intermediate values of ϕ_A and n_p to converge to the same level (i.e. 10^{-6}). However, increasing ϕ_A or n_p does not require a significant increase of the iterations in Figs 12(c) and (d) in contrast to the simplified equations. This suggests that the iteration solving the coupling of two sets of equations also help to improve the convergence of the non-linearity in our PT method.

5 DISCUSSION

5.1 The genesis of fluid channels

Our numerical models allow us to explore the fundamental reasons for generating fluid channels in the two-phase system, from simplified equations to full equations. First, our 1-D simplified models confirm that decompaction weakening is essential (Connolly & Podladchikov 2007; Räss *et al.* 2019) because it produces vertically elongated porosity profiles (Fig. 3). Fluid can only slowly penetrate through the background material without decompaction weakening ($R = 1$) (Figs 3d and 10d) as reported in previous studies (e.g. Dohmen *et al.* 2019). The 2-D simplified models with different reservoir topographies show that the geometry of the reservoir plays an important role in channel initiation. However, fluid channels can develop without any initial topographic features, manifesting the two-phase system's flow instability. We further explore this flow instability with the full equations that include the effects of shear stress (Fig. 5). By comparing models with three different background porosities, we find flow instability and fluid channels develop faster and easier with low shear stress in general, although a high background porosity ($\phi_0 = 0.1$) also makes a difference (i.e. Fig. 5f). In fact, the full equations reduce to the simplified equations when the shear viscosity approaches zeros. These models help us also clarify that it the actual ratio between the shear viscosity and bulk viscosity ($\frac{\phi^0}{C}$) that matters for the development of flow instability and fluid channels. A smaller viscosity ratio leads to easier and faster flow instability development. Therefore, we understand

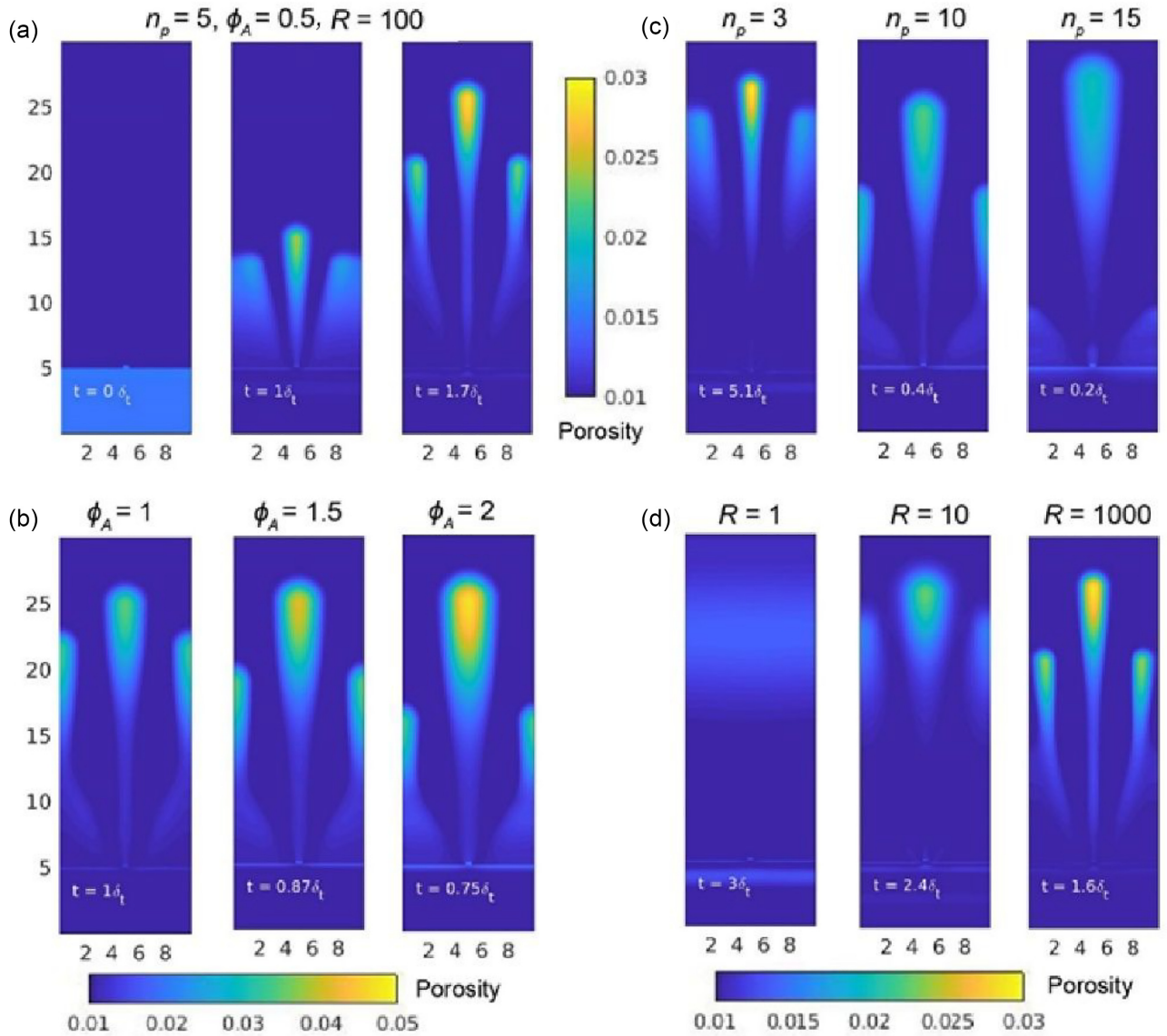


Figure 10. Fluid channel development with different permeability exponents (n_p), porosity contrast (ϕ_A) and R factors. (a) The porosity evolution of the model with $n_p = 5$, $\phi_A = 0.5$ and $R = 100$. (b) The porosity fields for models with different ϕ_A when the porosity wave reaches $z = 26$. (c) The porosity field for models with different n_p that controls the width of the channels and the speed of channel development. (d) The porosity field for models with different R values that impact whether the localized fluid channels form or not. The model in Fig. 10(a) serves as a reference model; we then varies ϕ_A , n_p and R in the model sets in Figs 10(b)–(d).

the reason for the locations where fluid channels are initiated: The flow instability is triggered by the initial topographic features and forms fluid channels, that are quickened by low shear viscosity. We further note that models with background porosity $\phi_0 = 0.01$ and $\phi_0 = 0.001$ show similar porosity patterns when the same ratio μ_s/η_ϕ is applied; while models with $\phi_0 = 0.1$ show rather different patterns in Fig. 5. This comparison is based on the compaction timescales scaled with background porosity (eq. 7), thus making the model time comparable. A similar observation is also found for 1-D models in Fig. 3, suggesting that model results for low porosity (i.e. $\phi_0 < 0.01$) could not mimic the dynamics of fluid flow with large porosity (i.e. $\phi_0 > 0.1$).

Besides the viscous bilinear rheology, the viscoplastic rheology that includes a dilation pressure can also produce fluid channels. Using this rheology, the dilation pressure helps open the pore-space,

requiring less weakening of the bulk viscosity (Yarushina *et al.* 2020). Figs 9(e) and (d) show that the viscoplastic rheology produces slightly higher porosity, while channel propagations can be as fast as the viscous bilinear models with $R = 100$ or 500. The advantage of viscoplastic rheology is that the negative effective pressure required for viscous bilinear rheology is no longer inevitable. This is consistent with the fact that plastic failure occurs when the fluid pressure is smaller than solid pressure in many situations (Jaeger *et al.* 2009). Thus, fluid channel development under a two-phase flow theory can be applied to many phenomena without negative effective pressure. Notice this viscoplastic rheology can also produce negative effective pressure when the rheological parameters are adjusted, as might be expected in hot magmatic rocks. Therefore, this rheology can include the applications of viscous bilinear rheology and more.

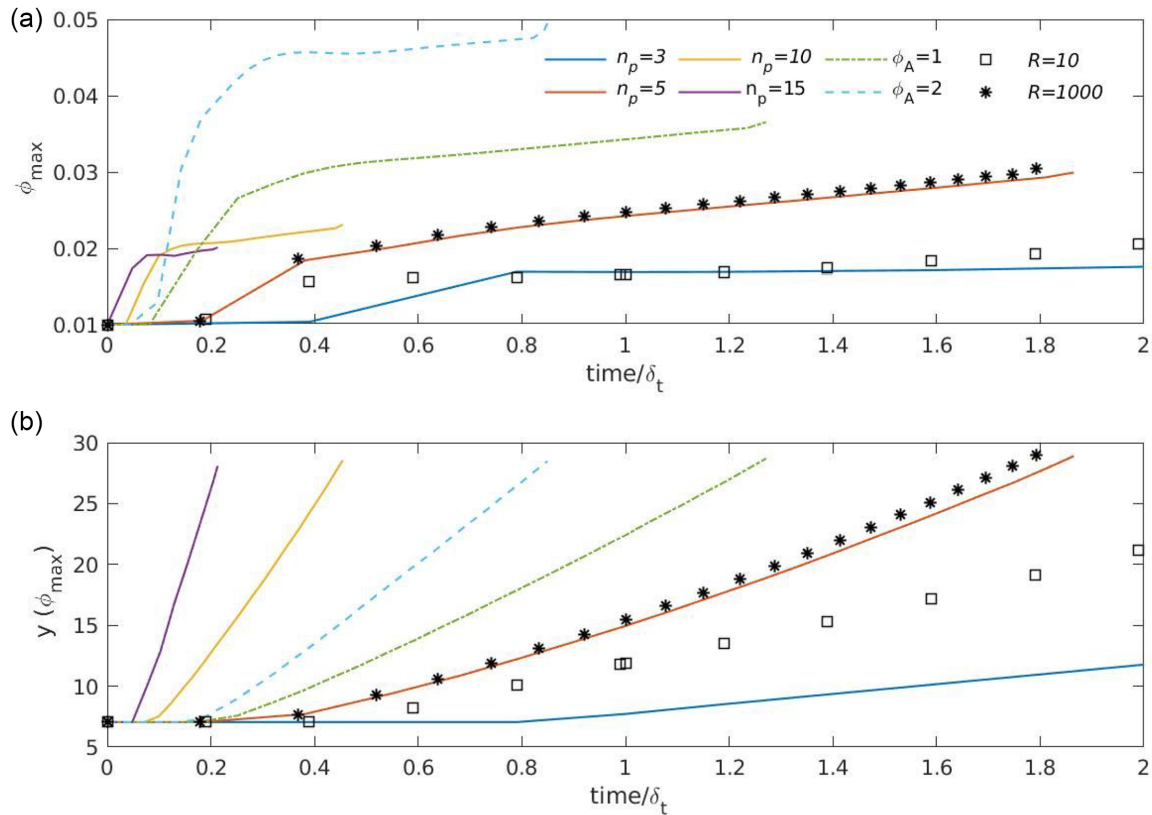


Figure 11. Evolution of maximum porosity (a) and its vertical location (b) for models with different permeability exponents n_p , porosity contrasts (ϕ_A) and R factors. These results are for the same sets of models as in Fig. 10.

5.2 Channel width and propagation speed

A wide range of initial conditions and parameters are tested in our models, which allows us to clarify the factors that control the size and speed of the channel propagation. First of all, our model domain is scaled with the background compaction length that depends on the background bulk viscosity, permeability and fluid viscosity (eq. 7). This means that the channel widths and spacing between channels depend on the background compaction length (Rass *et al.* 2019). The compaction length might change due to the existence of a new geological layer, which can be more viscous and less permeable. Figs 8(a) and (b) shows that the channels become wider in a strong layer (high bulk viscosity) and narrower in a weak layer, suggesting that local variation of bulk viscosity affects the widths of the local channels. In other words, channel widths change when the channel penetrates a geological layer with different viscosity. Figs 8(c) and (d) shows that a geological layer with different permeability can significantly change the channel widths and propagation speed. The development of the fluid channels is largely restrained by the low permeability layer but did not completely stop (see supplementary material). Our models find interesting dynamics when fluid channels meet a different geological layer, including changes in the channel width and propagation speed. This finding is important for modelling channel development in a real geological setting that involves reservoir rock, intraformational rock and caprock (Elenius *et al.* 2018).

Based on the length unit defined by background compaction length, we can evaluate how the rock properties affect the width and propagation speed of the channels. Shear viscosity alone can also play a role without changing compaction length, as shown by

the model comparison in Fig. 5. Models with a high shear viscosity (Figs 5d, b and c) have no clear localized channel, indicating potentially wider channels than the model domain. The fluid channels narrow down into 2–4 in models with a 10-fold lower shear viscosity (Figs 5a, e and f). We also noticed that the effects on the propagation speed are minor. Nevertheless, both the channel width and propagation speed increase significantly when the permeability exponent increases from 3 to 15. The channel width increases from ~ 2 for $n_p = 3$ to ~ 4 for $n_p = 15$, while the speed of the channel propagation increases by ~ 25 times (Fig. 10c). This change in the speed is dominant over other parameters such as ϕ_A , R , and initial anomaly. This finding has important implications for fluid leakage from the caprock.

Besides the rock properties, our models also show that the widths of the fluid channels vary due to the initial geometry of the reservoir. Fig. 4 shows that the initial curvature affects not only the location of the channels but also the width, strength and propagation speed. The reservoir feeds into one single strong channel with $X_a = 8$, while only two narrow and weak channels are observed for the model with a flat surface, as shown in Figs 4a) and d). Such variations in the channel widths are also observed for models with full equations in Figs 6(a) and (b). These models also show that the dynamics of one wide topographic feature develop into two separate channels (Fig. 6a) and two close features develop into one single channel (Fig. 6b). Models with a sinusoidal reservoir show that reservoir geometry and discretization play important roles in the channel widths. Due to the limited resolution, the initial reservoir geometry is defined by the wavenumber of the sinusoidal function and the jagged structures from the discretization. A large and intermediate

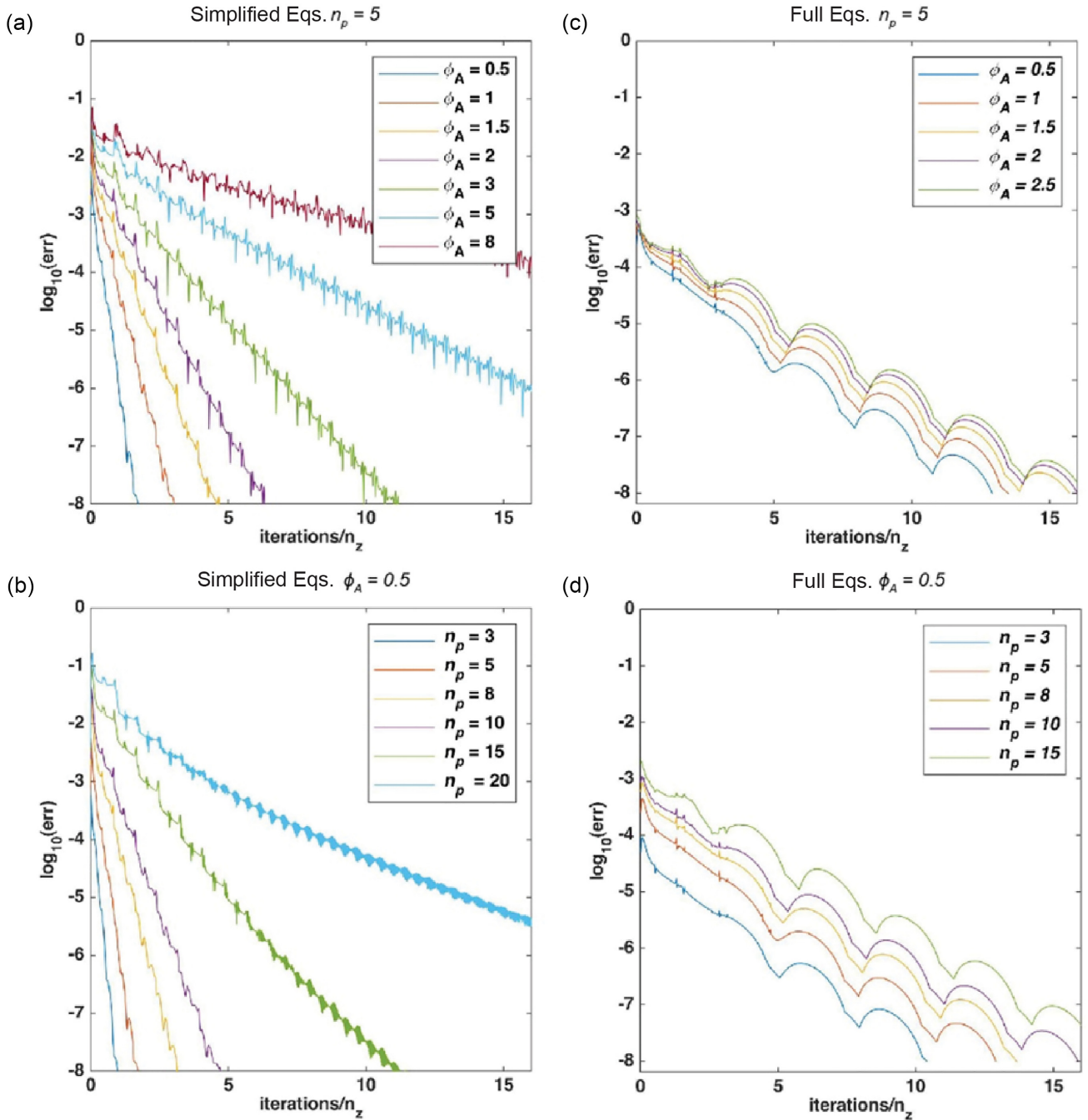


Figure 12. The numerical convergence of the proposed pseudo-transient method for 1-D simplified equations (a, c) and 2-D full equations (b, d). We choose the 2nd step calculation to show the convergence through iterations. The background porosity is 0.01. (a) The convergence for 1-D simplified equations with different porosity contrasts from $\phi_A = 0.5$ to $\phi_A = 8$ times with $n_p = 5$. (b) The convergence for a 1-D simplified equations with different permeability exponents from $n_p = 3$ to 20 with $\phi_A = 0.5$. (c) The convergence for 2-D full equations with different ϕ_A values (from 0.5 to 2.5) with $n_p = 5$. (d) The convergence for 2-D full equations with different n_p (from 3 to 15) with $\phi_A = 0.5$.

wavenumber ($k_w = 8$ and 4) causes many small topographical features to be created close to each other, leading to the merging of the fluid channels at the peaks of the initial geometry (Figs 7a–c, d). The model with $k_w = 4$ has much wider but weaker channels than models with $k_w = 8$. At a small wavenumber ($k_w = 2$), the initial geometry’s jagged structure is wide enough to develop one or two channels by itself but does not merge with each other (Figs 7e and f), thus leading to weak channels. Therefore, one single channel would be formed when the width of the bump structure in the reservoir

is comparable to or smaller than compaction length, while several channels might be formed when the bump width is much larger than the compaction length.

5.3 Physics-inspired numerical techniques

With numerical techniques developed from physical intuition, our numerical method pushes the performance limits in terms of the

necessary iteration number. For the simplified equations, we aim to use as large pseudo step ($\Delta\tau_{pe}$) as possible in eq. (27) (i.e. X_d close to 1) while maintaining stabilization of the iterations (pseudo time-stepping). By applying local V_p and ρ_n for every node, we were able to use X_d close to 1 (e.g. $X_d = 1.1$) for some calculations. However, the pseudo time-stepping would still diverge quickly when the permeability contrast is large (e.g. high n_p and ϕ_A). This phenomenon motivates us to apply the minimum $\Delta\tau_{pe}$ from the neighbourhood of every node. We found that it is tremendously helpful for the stabilization, as it enables us to use $X_d = 1.1$ for high permeability contrast ($(1 + \phi_A)^{np}$) up to 10^5 . Nevertheless, it is still useful to use slightly larger X_d values when the resolution is comparably low for the local permeability contrast. Figs 12(a) and (b) shows the convergences for n_p up to 20 when $\phi_A = 0.5$ and ϕ_A up to 8 when $n_p = 5$ under the current resolution. We can use similar techniques in eq. (30) for the full equations, for example applying local values for shear viscosity μ_s . As shear viscosity is constant through time in our models, this is unnecessary for most of our models, except for the models with weaker or strong layers in Fig. 8. More numerical techniques can be developed from the physical intuition of wave propagation.

For the full equations, we found that the numerical processes of the two damping schemes couple well with each other to form a pseudo-transient solver for the two-phase flow system. No significant change is required when the two damping schemes are applied together for the full equations. The simplified equations help us understand the physics of porosity waves; similarly, the experience of solving the simplified equations is also useful for solving the full equations. The same techniques obtained from the simplified equations can be used directly. Nevertheless, tuning the parameters (i.e. X_d , X_p , X_v) for better convergence is necessary. For example, we find it converges much faster when $X_d = 2$ is used than $X_d = 1.1$ sometimes, indicating that $X_d = 1.1$ is no longer necessarily optimal for the full equations. Comparing the convergence of simplified and full equations in Fig. 12, it is not surprising that solving the full equations requires more iterations. However, we also find that the required iterations for the full equations do not increase as much as the simplified equations when the permeability contrast increases. This is an encouraging finding for solving the full coupling equations with high non-linearity. There is still plenty of room to improve since we did not aim to find the best parameters for each model in Figs 12(c) and (d). Rather, we show that our method can handle large contrasts and non-linearity. For example, changing X_p through iterations can gradually accelerate the convergence (see the code for implementation). Adjusting η_b based on the magnitude of shear viscosity μ_s is also helpful when different shear viscosity values are applied. It requires experience to find good combinations of parameters and develop specific techniques, which is inevitable for solving complex non-linear problems.

The accuracy and performance of the pseudo-transient method on solving the 2-D/3-D two-phase system have been well demonstrated upon comparison with a direct method (Rass *et al.* 2019). The pseudo-transient solver can solve the equations as accurately as the direct-iterative solver. It can also scale much better when the total number of nodes increases, especially for the 3-D problem. Our study further confirms that the necessary iteration can be reduced to $O(n_i)$ with proper damping schemes, while n_i is the number of cells in the i direction. Therefore, if N is the total number of the nodes, then the required iterations are $O(N)$, $O(N^{1/2})$, and $O(N^{1/3})$ for 1D, 2D, and 3D problems, respectively. The total computation complexity of one time-stepping for 1-D, 2-D and 3-D problems are \sim

$O(N^2)$, $O(N^{3/2})$ and $N^{4/3}$, respectively. This is especially meaningful for large 3-D numerical problems.

5.4 Implications for future work

Geological applications of porosity waves usually involve different material properties for different layers as well as non-linear shear viscosity. Models with a special layer (a contrast of 10 for permeability and viscosities) show that our method can handle the high permeability contrast caused by non-linearity as well as the material difference by using local values of permeability, bulk viscosity, and shear viscosity in the pseudo-transient stepping. However, more work is required to deal with even larger contrast (e.g. permeability contrast values of more than 100 or 1000). These would likely require increasing resolutions according to the local compaction length and would be useful for studies of the storage and leakage of the reservoir under the caprock that involves a few orders of permeability difference. This new viscoplastic rheology allows us to apply our models directly to geological applications by providing rheological formulations and parameters based on experimental data (Yarushina *et al.* 2020). We expect that modelling results can match observations better than before, including not only the porosity and permeability fields but also the stress and pressure fields. Thus, more efforts are needed to study porosity wave behaviour with the viscoplastic rheology for different geological applications.

Our study shows that PT continuation for the complex coupled system can be built up from numerical techniques for the simplified systems. Similar to how the physical equations can couple each other, the damping schemes can also couple to solve the equations, as shown in our approach. That is, by developing numerical techniques separately for simple equations, we can further solve the coupled system with relatively limited modifications. Therefore, we expect this type of PT method inspired by physics to be applied to more research fields that require the complex coupled system to be solved.

6 CONCLUSION

Through numerical theory and examples, this study provides a solution to the two-phase flow problem for both simplified decoupled equations and full two-phase flow equations via a matrix-free pseudo-transient method. With the simplified equation that ignores shear stress, we explore the effects of background porosity, decompaction weakening factors, porosity contrast and permeability exponents. We found that the decompaction weakening is necessary to elongate the porosity profile, and permeability exponents play the dominant role in the speed of wave propagation. With 2-D models for both simplified equations and full equations, we clarify that localized fluid channels are the natural outcome of the flow instability of the two-phase system that has a low ratio (<0.1) between shear viscosity and bulk viscosity. This is independent of the initial reservoir geometry. However, the reservoir's initial geometry affects the location of the channels by providing initial structure/irregularity on which the flow instability can be built. 2-D models for full two-phase flow equations also confirm the effects of decompaction weakening and permeability exponents found by simplified models. Scaled with compaction length, the sizes of the channels are found to depend on other many factors in our models, such as shear viscosity, permeability exponents and channels numbers. We further test the effects of a layer with different viscosities and permeabilities and

find that the sizes and propagation speeds of the channels are adjusted accordingly in the layer. We perform numerical models with the new viscoplastic rheology and show that the negative effective pressure is not necessary for the porosity waves. These findings further certify the porosity wave of the two-phase (solid + fluid) flow system as a promising way to study fluid flow in real geological settings, such as subsurface reservoirs and caprock.

The physics of damped wave were used to provide a simple explanation of all the steps involved in the development of a pseudo-transient method for various types of equations. We show that the numerical scheme for complex coupled systems can be assembled by damping schemes for each simple system with little modification. By performing simulation using different equations, model setups, and parameters, we also demonstrate the capacity and efficiency of our pseudo-transient method. Applying local values for the variables such as permeability, bulk viscosity, shear viscosity in the iteration processes enable us to speed up the convergence. As we show, many numerical techniques can be developed and applied based on the physical intuitions of the wave damping process due to the simplicity and readability of the code. We encourage the reader to explore these numerical techniques by using the provided Matlab codes (<https://doi.org/10.5281/zenodo.4790635>)

ACKNOWLEDGEMENTS

Lawrence H. Wang and Viktoriya Yarushina are funded by the project ‘CO2-Paths’ (grant No. 280567) from Research Council of Norway. We thank Magnus Wangen for his supports and discussion in this project. Yury Y. Podladchikov and Yury Alkhimenkov acknowledge support from the Ministry of Science and Higher Education of the Russian Federation (Project No. 075–15–2019–1890). Yury Alkhimenkov gratefully acknowledges support from the Swiss National Science Foundation, project number 172691.

DATA AVAILABILITY

No specific data is used in this study. For the reproducibility of the presented results, we provide the Matlab codes for both algorithm analysis and two-phase flow modelling through a DOI repository (<https://doi.org/10.5281/zenodo.4790635>).

REFERENCES

- Alkhimenkov, Y., Khakimova, L. & Podladchikov, Y., 2021. Stability of discrete schemes of Biot's poroelastic equations, *Geophys. J. Int.*, **225**, 354–377.
- Appold, M.S. & Nunn, J.A., 2002. Numerical models of petroleum migration via buoyancy-driven porosity waves in viscously deformable sediments, *Geofluids*, **2**, 233–247.
- Audet, D.M. & Fowler, A.C., 1992. A mathematical model for compaction in sedimentary basins, *Geophys. J. Int.*, **110**, 577–590.
- Audet, P., Bostock, M.G., Christensen, N.I. & Peacock, S.M., 2009. Seismic evidence for overpressured subducted oceanic crust and megathrust fault sealing, *Nature*, **457**, 76–78.
- Bauer, S., Huber, M., Ghelichkhan, S., Mohr, M., Rüde, U. & Wohlmuth, B., 2019. Large-scale simulation of mantle convection based on a new matrix-free approach, *J. Comput. Sci.*, **31**, 60–76.
- Benjamin, M., Calder, J., Sundaramoorthi, G. & Yezzi, A., 2020. Accelerated variational PDEs for efficient solution of regularized inversion problems, *J. Math. Imaging Vis.*, **62**, 10–36.
- Bercovici, D., Ricard, Y. & Schubert, G., 2001. A two-phase model for compaction and damage: 1. General Theory, *J. geophys. Res.*, **106**, 8887.
- Burov, E., Francois, T., Yamato, P. & Wolf, S., 2014. Advances and challenges in geotectonic modelling, *Bull. la Soc. Geol. Fr.*, **185**, 147–169.
- Burov, E., Jolivet, L., Le Pourhiet, L. & Poliakov, A., 2001. A thermomechanical model of exhumation of high pressure (HP) and ultra-high pressure (UHP) metamorphic rocks in Alpine-type collision belts, *Tectonophysics*, **342**(1–2), 113–136.
- Cai, Z. & Bercovici, D., 2013. Two-phase damage models of magma fracturing, *Earth planet. Sci. Lett.*, **368**, 1–8.
- Calder, J. & Yezzi, A., 2018. PDE Acceleration: a convergence rate analysis and applications to obstacle problems, *Res. Math. Sci.*, **6**, Retrieved from, <http://arxiv.org/abs/1810.01066>.
- Calder, J. & Yezzi, A., 2019. PDE acceleration: a convergence rate analysis and applications to obstacle problems, *Res. Math. Sci.*, **6**, 35, doi:10.1007/s40687-019-0197-x.
- Chen, J., 2009. Pseudo-transient continuation-based variable relaxation solver in nonlinear magnetohydrodynamic simulations, *Int. J. Comput. Math.*, **86**, 1473–1482.
- Clevenger, T.C. & Heister, T., 2019. Comparison between algebraic and matrix-free geometric multigrid for a Stokes problem on adaptive meshes with variable viscosity, Retrieved from, <http://arxiv.org/abs/1907.06696>.
- Connolly, J. A. D. & Podladchikov, Y.Y., 2000. Temperature-dependent viscoelastic compaction and compartmentalization in sedimentary basins, *Tectonophysics*, **324**, 137–168.
- Connolly, J. & Podladchikov, Y., 1998. Compaction-driven fluid flow in viscoelastic rock, *Geodin. Acta*, **11**, 55–84.
- Connolly, J.A.D. & Podladchikov, Y.Y., 2007. Decompaction weakening and channeling instability in ductile porous media: implications for asthenospheric melt segregation, *J. geophys. Res.*, **112**, B10205. doi:10.1029/2005JB004213.
- Costa, A., 2006. Permeability-porosity relationship: a reexamination of the Kozeny-Carman equation based on a fractal pore-space geometry assumption, *Geophys. Res. Lett.*, **33**(2), doi:10.1029/2005GL025134.
- Cundall, P. A., 1989. Numerical experiments on localization in frictional materials, *Ing.-Arch.*, **59**, 148–159.
- Dannberg, J. & Heister, T., 2016. Compressible magma/mantle dynamics: 3-D, adaptive simulations in ASPECT, *Geophys. J. Int.*, **207**, 1343–1366, Oxford University Press.
- Dohmen, J., Schmeling, H. & Kruse, J.P., 2019. The effect of effective rock viscosity on 2-D magmatic porosity waves, *Solid Earth*, **10**, 2103–2113, Copernicus GmbH.
- Duretz, T., Räss, L., Podladchikov, Y.Y. & Schmalholz, S.M., 2019. Resolving thermomechanical coupling in two and three dimensions: spontaneous strain localization owing to shear heating, *Geophys. J. Int.*, **216**, 365–379.
- Duretz, T., Souche, A., de Borst, R. & Le Pourhiet, L., 2018. The benefits of using a consistent tangent operator for viscoelastoplastic computations in geodynamics, *Geochem., Geophys. Geosyst.*, **19**, 4904–4924.
- Elenius, M. et al., 2018. Assessment of CO2 storage capacity based on sparse data: skade formation, *Int. J. Greenh. Gas Control*, **79**, 252–271, Elsevier Ltd.
- Frankel, S.P., 1950. Convergence rates of iterative treatments of partial differential equations, *Math. Comput.*, **4**, 65–65.
- Jaeger, J., Cook, N. & Zimmerman, R., 2009. *Fundamentals of Rock Mechanics*, 4th edn., Retrieved from, <https://www.wiley.com/en-us/Fundamentals+of+Rock+Mechanics%2C+4th+Edition-p-9780632057597>.
- Ji, L., Settari, A. & Sullivan, R.B., 2009. A novel hydraulic fracturing model fully coupled with geomechanics and reservoir simulation, *SPE J.*, **14**, 423–430.
- Jordan, J.S., Hesse, M.A. & Rudge, J.F., 2018. On mass transport in porosity waves, *Earth planet. Sci. Lett.*, **485**, 65–78.
- Katz, R.F., Spiegelman, M. & Holtzman, B., 2006. The dynamics of melt and shear localization in partially molten aggregates, *Nature*, **442**, 676–679.
- Keller, T., May, D.A. & Kaus, B.J.P., 2013. Numerical modelling of magma dynamics coupled to tectonic deformation of lithosphere and crust, *Geophys. J. Int.*, **195**, 1406–1442.
- May, D. A., Brown, J. & Le Pourhiet, L., 2015. A scalable, matrix-free multigrid preconditioner for finite element discretizations of heterogeneous Stokes flow, *Comput. Methods Appl. Mech. Eng.*, **290**, 496–523.

- May, D.A., Brown, J. & Le Pourhiet, L., 2014. PTatin3D: high-performance methods for long-term lithospheric dynamics, in *SC '14: Proceedings of the International Conference for High Performance Computing, Networking, Storage and Analysis*, 16–21 November 2014, New Orleans, LA, USA, pp. 274–284, doi:10.1109/SC.2014.28, IEEE.
- Mckenzie, D., 1984. The generation and compaction of partially molten rock, *J. Petrol.*, **25**, 713–765.
- Morency, C., Huismans, R.S., Beaumont, C. & Fullsack, P., 2007. A numerical model for coupled fluid flow and matrix deformation with applications to disequilibrium compaction and delta stability, *J. geophys. Res.*, **112**, B10407, doi:10.1029/2006JB004701.
- Moresi, L., Betts, P.G., Miller, M.S. & Cayley, R.A., 2014. Dynamics of continental accretion, *Nature*, **508**, 245–248.
- Morra, G., 2020. *Extended Abstract: Fresh Outlook in Numerical Methods for Geodynamics*, Vol. 70, GCAGS Transactions. Retrieved from, http://archives.datapages.com/data/gcags/data/070/070001/269_gcags700269.htm.
- Omlin, S., Räss, L. & Podladchikov, Y.Y., 2018. Simulation of three-dimensional viscoelastic deformation coupled to porous fluid flow, *Tectonophysics*, **746**, 695–701.
- Otter, J.R.H., Cassell, A.C. & Hobbs, R.E., 1966. Dynamic relaxation, *Proc. Inst. Civ. Eng.*, **35**, 633–656.
- Petrini, C., Gerya, T., Yarushina, V., Dinther, Y. van, Connolly, J. & Madonna, C., 2020. Seismo-hydro-mechanical modelling of the seismic cycle: methodology and implications for subduction zone seismicity, *Tectonophysics*, **791**, doi:10.1016/j.tecto.2020.228504.
- Poliakov, A.N.B., Cundall, P.A., Podladchikov, Y.Y. & Lyakhovskiy, V.A., 1993. An explicit inertial method for the simulation of viscoelastic flow: an evaluation of elastic effects on diapiric flow in two- and three- layers models, in *Flow and Creep in the Solar System: Observations, Modeling and Theory*, Stone, D.B. & Runcorn, S.K., Vol. 391, NATO ASI Series C, pp. 175–195, Springer, doi:10.1007/978-94-015-8206-3_12.
- Prevost, J.H., 2014. Two-way coupling in reservoir-geomechanical models: vertex-centered Galerkin geomechanical model cell-centered and vertex-centered finite volume reservoir models, *Int. J. Numer. Methods Eng.*, **98**, 612–624.
- Räss, L., Duretz, T. & Podladchikov, Y.Y., 2019. Resolving hydromechanical coupling in two and three dimensions: spontaneous channelling of porous fluids owing to decompaction weakening, *Geophys. J. Int.*, **218**, 1591–1616.
- Räss, Ludovic, Simon, N.S.C. & Podladchikov, Y.Y., 2018. Spontaneous formation of fluid escape pipes from subsurface reservoirs, *Sci. Rep.*, **8**, 1–11.
- Räss, Ludovic, Yarushina, V.M., Simon, N.S. & Podladchikov, Y.Y., 2014. Chimneys, channels, pathway flow or water conducting features - an explanation from numerical modelling and implications for CO₂ storage, *Ener. Proc.*, **63**, 3761–3774.
- Revil, A., 2002. Genesis of mud volcanoes in sedimentary basins: a solitary wave-based mechanism, *Geophys. Res. Lett.*, **29**, 1574.
- Rice, J.R., 1992. Fault stress states, pore pressure distributions, and the weakness of the San Andreas Fault, *Int. Geophys.*, **51**, 475–503.
- Rinaldi, A.P., Rutqvist, J., Luu, K., Blanco-Martín, L., Hu, M. & Sentis, M.L., 2021. TOUGH3-FLAC3D: a modeling approach for parallel computing of fluid flow and geomechanics, *Earth Space Sci. Open Arch.*, **27**, doi:10.1002/ESSOAR.10505967.1.
- Sabitova, A. et al., 2021, Experimental Compaction and Dilation of Porous Rocks During Triaxial Creep and Stress Relaxation, *Rock Mech. and Rock Engineering*, **54**, 5781–5805, doi.org/10.1007/s00603-021-02562-4.
- Schmeling, H. & Wallner, H., 2012. Magmatic lithospheric heating and weakening during continental rifting: a simple scaling law, a 2-D thermo-mechanical rifting model and the East African Rift System, *Geochem., Geophys. Geosyst.*, **13**, doi:10.1029/2012GC004178.
- Settari, A. & Walters, D.A., 2001. Advances in coupled geomechanical and reservoir modeling with applications to reservoir compaction, *SPE J.*, **6**, 334–342.
- Spitz, R., Bauville, A., Epard, J.-L., Kaus, B.J.P., Popov, A.A. & Schmalholz, S.M., 2020. Control of 3-D tectonic inheritance on fold-and-thrust belts: insights from 3-D numerical models and application to the Helvetic nappe system, *Solid Earth*, **11**, 999–1026.
- Tackley, P.J., 2008. Modelling compressible mantle convection with large viscosity contrasts in a three-dimensional spherical shell using the yin-yang grid, *Phys. Earth planet. Inter.*, **171**, 7–18.
- Takei, Y. & Richard, F.Katz, 2013. Consequences of viscous anisotropy in a deforming, two-phase aggregate. Part 1. Governing equations and linearized analysis, *Journal of Fluid Mechanics*, **734**, 424–455, doi.org/10.1017/jfm.2013.482.
- Tarokh, A., Makhnenko, R.Y., Kim, K., Zhu, X., Popovics, J.S., Segvic, B. & Sweet, D.E., 2020. Influence of CO₂ injection on the poromechanical response of Berea sandstone, *Int. J. Greenh. Gas Control*, **95**, doi:10.1016/j.ijggc.2020.102959.
- Vasilyev, O.V., Podladchikov, Y.Y. & Yuen, D.a., 1998. Modeling of compaction driven flow in poro-viscoelastic medium using adaptive wavelet collocation method, *Geophys. Res. Lett.*, **25**, 3239–3242.
- Wang, H., Huismans, R.S. & Rondenay, S., 2019. Water migration in the subduction mantle wedge: a two-phase flow approach, *J. geophys. Res.*, **124**, 9208–9225.
- Wangen, M., 2011. Finite element modeling of hydraulic fracturing on a reservoir scale in 2D, *J. Pet. Sci. Eng.*, **77**, 274–285.
- Yarushina, V.M., Podladchikov, Y.Y. & Wang, L.H., 2020. Model for (De)Compaction and Porosity Waves in Porous Rocks Under Shear Stresses, *J. of Geophys. Res.: Solid Earth*, **125**(8), doi.org/10.1029/2020JB019683.
- Yarushina, V.M., Dabrowski, M. & Podladchikov, Y.Y., 2010. An analytical benchmark with combined pressure and shear loading for elastoplastic numerical models, *Geochem., Geophys. Geosyst.*, **11**, doi:10.1029/2010GC003130.
- Yarushina, Viktoriya M., Bercovici, D. & Oristaglio, M.L., 2013. Rock deformation models and fluid leak-off in hydraulic fracturing, *Geophys. J. Int.*, **194**, 1514–1526.
- Yarushina, Viktoriya M. & Podladchikov, Y.Y., 2015. (De)compaction of porous viscoelastoplastic media: model formulation, *J. geophys. Res.*, **120**, 4146–4170.
- Zhang, L.G. & Yu, T.X., 1989. Modified adaptive Dynamic Relaxation method and its application to elastic-plastic bending and wrinkling of circular plates, *Comput. Struct.*, **33**, 609–614.
- Zheng, L., May, D., Gerya, T. & Bostock, M., 2016. Fluid-assisted deformation of the subduction interface: coupled and decoupled regimes from 2-D hydromechanical modeling, *J. geophys. Res.*, **121**, 6132–6149.
- Zhong, S., Zuber, M.T., Moresi, L. & Michael, G., 2000. Role of temperature-dependent viscosity and surface plates in spherical shell models of mantle convection, *J. geophys. Res.*, **105**, 11 063–11082.

SUPPORTING INFORMATION

Supplementary data are available at *GJI* online.

AppendixV2.docx

SuppVideos.zip

Please note: Oxford University Press is not responsible for the content or functionality of any supporting materials supplied by the authors. Any queries (other than missing material) should be directed to the corresponding author for the paper.